ORNL/TM-2024/3436

STRUCTURAL HEALTH MONITORING FOR LARGE-SCALE ADDITIVE MANUFACTURING USING ACOUSTIC EMISSION TECHNIQUE

Ryan Spencer
Miguel González Núñez
Adwoa Owusu
Hossain Saboonchi
Valery Godinez-Azcuagu
Uday K. Vaidya
Vlastimil Kunc
Ahmed Arabi Hassen

CRADA FINAL REPORT
NFE-20-07989

Approved for Public Release
Distribution is Unlimited

June 2024

OAK RIDGE National Laboratory

ORNL IS MANAGED BY UT-BATTELLE LLC FOR THE US DEPARTMENT OF ENERGY

DOCUMENT AVAILABILITY

Reports produced after January 1, 1996, are generally available free via OSTI.GOV.

Website www.osti.gov

Reports produced before January 1, 1996, may be purchased by members of the public from the following source:

National Technical Information Service
5285 Port Royal Road
Springfield, VA 22161
Telephone 703-605-6000 (1-800-553-6847)
TDD 703-487-4639
Fax 703-605-6900
E-mail info@ntis.gov
Website http://classic.ntis.gov/

Reports are available to DOE employees, DOE contractors, Energy Technology Data Exchange representatives, and International Nuclear Information System representatives from the following source:

Office of Scientific and Technical Information
PO Box 62
Oak Ridge, TN 37831
Telephone 865-576-8401
Fax 865-576-5728
E-mail reports@osti.gov
Website https://www.osti.gov/

This report was prepared as an account of work sponsored by an agency of the United States Government. Neither the United States Government nor any agency thereof, nor any of their employees, makes any warranty, express or implied, or assumes any legal liability or responsibility for the accuracy, completeness, or usefulness of any information, apparatus, product, or process disclosed, or represents that its use would not infringe privately owned rights. Reference herein to any specific commercial product, process, or service by trade name, trademark, manufacturer, or otherwise, does not necessarily constitute or imply its endorsement, recommendation, or favoring by the United States Government or any agency thereof. The views and opinions of authors expressed herein do not necessarily state or reflect those of the United States Government or any agency thereof.

ORNL/TM-2024/3436

Manufacturing Science Division

IN-PROCESS MONITORING AND STRUCTURAL HEALTH MONITORING OF LARGE-SCALE ADDITIVE MANUFACTURING USING ACOUSTIC EMISSION TECHNIQUE

Ryan Spencer
Miguel González Núñez†
Adwoa Owusu
Hossain Saboonchi†
Valery Godinez-Azcuagu†
Uday K. Vaidya
Vlastimil Kunc
Ahmed Arabi Hassen

† MISTRAS Group

June 2024

Prepared by
OAK RIDGE NATIONAL LABORATORY
Oak Ridge, TN 37831
managed by
UT-BATTELLE LLC
for the
US DEPARTMENT OF ENERGY
under contract DE-AC05-00OR22725

CONTENTS

LIST OF FIGURES

ACKNOWLEDGEMENTS

This CRADA NFE-20-07989 was conducted as a Technical Collaboration project within the Oak Ridge National Laboratory (ORNL) Manufacturing Demonstration Facility (MDF) sponsored by the US Department of Energy Advanced Manufacturing Office (CPS Agreement Number 24761). Opportunities for MDF technical collaborations are listed in the announcement "Manufacturing Demonstration Facility Technology Collaborations for US Manufacturers in Advanced Manufacturing and Materials Technologies" posted at http://web.ornl.gov/sci/manufacturing/docs/FBO-ORNL-MDF-2013-2.pdf. The goal of technical collaborations is to engage industry partners to participate in short-term, collaborative projects within the Manufacturing Demonstration Facility (MDF) to assess applicability and of new energy efficient manufacturing technologies. Research sponsored by the U.S. Department of Energy, Office of Energy Efficiency and Renewable Energy, Advanced Manufacturing Office, under contract DE-AC05-00OR22725 with UT-Battelle, LLC.

The authors would like to thank Dr. Uday Vaidya for facilitating multiple experiments at the Fibers and Composites Manufacturing Facility (FCMF) at the University of Tennessee, Knoxville. We also acknowledge and thank Eilish Stanek for performing experimentation and data analysis.

ABSTRACT

ORNL collaborated with MISTRAS Group, Inc. to investigate acoustic emission (AE) as a structural health monitoring (SHM) method for large-scale additive manufacturing (AM). Large-scale AM is being adapted as method of producing large structures in a short lead time and cost-effective way. With the growing advancement in AM techniques and application, machine monitoring and part qualification is highly needed. There has been leading research focused on the manufacturing, feedstock material but minimum research on the SHM, defect detection, and nondestructive evaluation (NDE) for AM. Scanning large structure using conventional nondestructive testing (NDT) techniques, such as ultrasound or X-ray, and searching for potential defects can be very time consuming, challenging and cost prohibitive. AE is a passive technique that can be used to monitor and locate defect progression in large structure by distributing group of sensors around the part. This project utilized AE technique and system manufactured/designed by MISTRAS Group to monitor large-scale AM equipment (i.e. Big Area Additive Manufacturing (BAAM) system located at the Oak Ridge National Laboratory – Manufacturing Demonstration Facility (ORNL-MDF) and the printed parts it produces. The AE system provided valuable insight on defect development/progression during and post-printing process.

1. ACOUSTIC EMISSION MONITORING ADDITIVE MANUFACTURING

MISTRAS Group is a leading "one source" multinational provider of integrated technology-enabled asset protection solutions, helping to maximize the safety and operational uptime for civilization's most critical industrial and civil assets. MISTRAS has ~5,400 employees across 115 locations worldwide, targeting key markets including oil & gas, aerospace, power, infrastructure, and manufacturing. Their consolidated sales nets to $270M USD.

In this technical collaboration work, three main investigations were accomplished: (1) understanding acoustic properties of common print material, (2) evaluating background noise of the AM system extruder and the gantry system, (3) perform sensor selection and sensor placement analysis, and (4) AE monitoring of crack development and verifying defect. The acoustic properties of the print material confirm AE can capture defect events with minimum attenuation. Evaluation of the waveforms and frequency response identifies which range of filters are necessary to eliminate the background noise for each print process. This work establishes the foundation for scaling up and validating the implementation of SHM-AE system for the large additive platform.

1.1 BACKGROUND

AM is a growing advanced manufacturing method that enables efficient fabrication for complex geometries by performing a layer-by-layer construction. The AM process still battles the control of defects including warpage, layer separation, internal voids, and cracking [1]. With large print volumes that can exceeds 1000 kg per part, detecting anomalies and discontinuities early on during the print process can reflect on corrective actions or stopping of inevitable print failure at early stages leading to significant saving on lead time, materials, and operation cost.

There are multiple applications which validate the implementation for the large-scale additive manufacturing, but the research in quality assurance is still in its early stages of research. There have been multiple NDE efforts for metal AM [2] [3] [4] and polymer AM [2] [5] [6] with most of the work performed on small scale (i.e. < 0.5 m^3) systems. There has been some NDE techniques that were used to investigate large-scale polymer AM [7, 8]. All examples display the ability for defect detection, but each NDE technique has their own limitation. As an example, infrared (IR) thermography must have the print within the field-of-view of the IR camera in order to monitor the print process. Ultrasound inspection is demonstrated as a post-process technique by detecting defects when the print is already

completed. A combination of different NDE techniques can lead to optimal detection of internal anomalies, residual warpage, interlayer separation and microcracking. There is a need for an in-situ monitoring technique that can detect printing anomalies before ultimate failure and allows for taking preventative action.

AE is a passive NDE technique by monitoring stress-related events caused by defects/anomalies such as crack nucleation and propagation within a structure [9] [10]. AE is a very well developed NDE method with ASTM standards [11] and ASME Code Section V, Articles 11 and 12 [12] developed for a wide range of applications. A common method of using AE is SHM for major assets including bridges [13], generators [14], wind turbine [15] [16], boilers and pipelines [17] [18]. The method is also used for material characterization including fatigue testing [19], impact detection [20] and fiber fracture within reinforced composites [21]. For Metal AM, AE has been utilized for in-situ monitoring [22]. AE has been adapted to monitor small scale polymer AM for health monitoring including filament feed breakage/slippage and process failure diagnosis [23] [24]. To the best of the author's knowledge, no research to adapt AE to large-scale polymer AM has been performed.

This work investigates the key fundamentals to utilize AE as a SHM technique for large-scale polymer and composites AM parts. This research investigates the AE signal attenuation for AM print materials and corresponding surface roughness, and the background noise signatures during normal operation for the extruder and gantry systems. The AE-based SHM system developed is expected to significantly improve the reliability and quality of large-scale AM processes. By providing early detection of defects and continuous monitoring of equipment health, this system will help minimize downtime, reduce material waste, and optimize production costs, ultimately leading to more robust and dependable large-scale additive manufacturing operations.

1.2 TECHNICAL RESULTS

1.2.1 Acoustic properties of AM composite materials

The materials used in this work were printed using the BAAM system at the ORNL-MDF. The BAAM equipment is a large-scale extrusion deposition AM system with a 6.1 m long, 2.4 m wide, and 1.8 m tall (20 ft x 8 ft x 6 ft) build envelope and extruder that is capable of deposition rates up to 50 kg/hr (110 lb/hr). Two different common polymers used within large-scale AM systems were investigated; an ABS reinforced with 20% fiber-weight-fraction carbon fiber (ABS/CF) and 50/50 polysulfone-polyethersulfone blend (PSU-PESU) reinforced with 25% fiber-weight-fraction CF (PSU-PESU/CF). ABS/CF is the most common and widely used material for large-scale AM for room temperature/low temperature applications (<100ºC) [25], where PSU-PESU/CF is commonly used for high-temperature applications and has low flammability features [26]. **Figure 1** shows the hexagon dimensions and the experimental procedures used for the AE attenuation study. The hexagon is a 431.8 mm (17 in) in length side-to-side and has a height of 254 mm (10 in) with a single wall thickness of 15.8 mm (0.625 in).

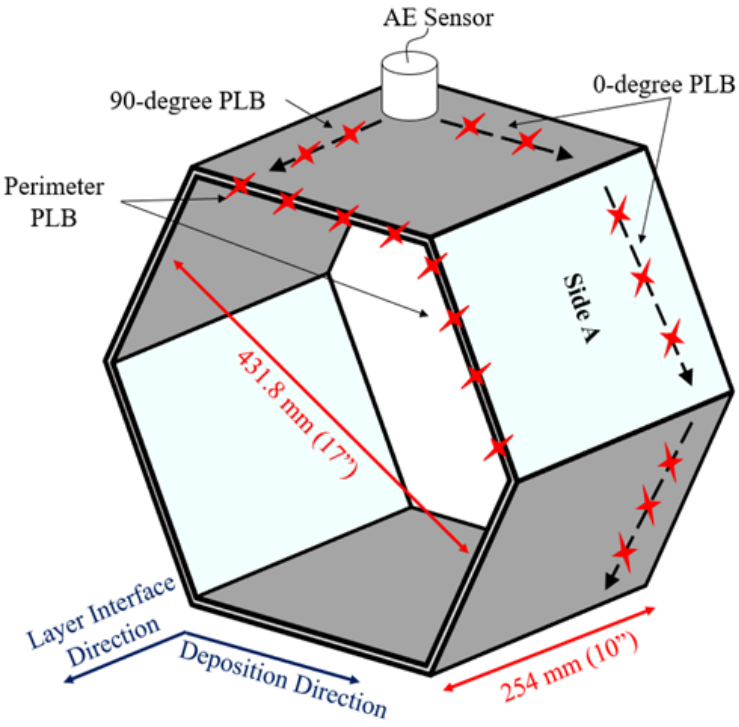

Figure 1: Schematic for the printed hexagon manufactured using the BAAM system showing sample dimension, printing orientation and coordinates and attenuation study setup with PLB excitation in the 0º direction, 90º direction, and perimeter direction directions to the sensor group placement

The AE testing was performed using a MISTRAS Group, Inc. Micro-II Digital AE system with selection of sensors listed in **Table 1** and associated preamplifiers. A wide selection of sensors is used in this research to provide a wide range of monitoring capability. Sensors with a resonant frequency provide high sensitivity at a narrow frequency range. These include the R.45I-LP-AST, PK3I, PK6I, and PK15I sensors. The PKBBI and PKWDI sensors are classified as broadband sensors with a wide operating frequency range. They typically have lower sensitivity than the resonant type sensors but benefit by monitoring a large frequency span. A sensor with acceptable amplification with minimum response decay over a distance is selected for monitoring the print material. All sensors are placed on the outside wall of the printed hexagon, shown in **Figure 1** and coupled with DOW CORNING – high vacuum silicon grease. The ABS/CF and PSU-PESU/CF hexagons went through multiple pencil lead break (PLB) excitations following ASTM E2374 which simulate micro-cracking [11]. The PLB excitations were performed using a Pentel P203 mechanical pencil with 2H, 0.3-mm diameter pencil lead. The attenuation study was performed by performing multiple PLBs and plotting the attenuation curve. The attenuation curve for each orientation (0º direction, 90º direction, and shear) were compared. Also, the surface roughness was investigated to see how the print surface effects the acoustic properties. Three different types of surface finishes were investigated (original print surface, locally-milled, and completely-milled).

Table 1: AE sensor identification and description

SENSOR ID	RESONANT FREQUENCY (KHZ)	OPERATING FREQUENCY RANGE (KHZ)	Features
R.45I-LP-AST	~4.5	1 – 30	Resonant very Low frequency (Audible) range
PK3I	~28	15 – 40	Resonant Low frequency (just above audible) range
PK6I	~55	35 – 85	Resonant Low-Medium frequency range
PK15I	150	80 – 450	Resonant Medium frequency range
PKBBI	NA	~20 – 600	Wideband Lower frequency range
PKWDI	NA	150 - 850	Wideband Higher frequency range

Attenuation Study

Attenuation study was performed in order to evaluate optimal sensor selection and the sensor spacing (i.e., location and placement) for large-scale AM print materials. The study also analyzed any anisotropic acoustic properties. Large-scale AM processes produce parts with anisotropic mechanical and thermal performance, due to the high fiber orientation in the direction of the deposition [27] [28] [29] [30]. Hence, we performed attenuation study in multiple orientations and directions in reference to the print direction, as shown in **Figure 1Error! Reference source not found.**. A PLB excitation was performed in 50 mm (2 in) increments along the deposition direction (0º direction), perpendicular to the deposition direction (90º direction), and along the edge of the sample (perimeter direction), see **Figure 1Error! Reference source not found.**. A PLB excitation was performed three times at each PLB distance to yield an average amplitude response. The test was repeated for each sensor type.

The attenuation results for ABS/CF and PSU-PESU/CF are shown in **Figure 2**. Each attenuation plot relates the distance a PLB excitation is away from the sensor position versus the amplitude response of each sensor caused by the distant excitation [17] [31]. For ABS/CF, the 0º direction the amplitude measurements at 50.8 mm (2 in) Source to Sensor Distance (SSD) are 79.3 dB, 94.0 dB, 92.0 dB, 80.7 dB, 83.7 dB and 78.7 dB for the PK6I, PK15I, PKBBI, PKWDI, R.45I-LP-AST, and PK3I, respectively. It can be noticed that the amplitude drops to 60.3 dB, 59.0 dB, 63.7 dB, 57.0 dB, 61.3 dB, and 61.7 dB for the sensors, respectively, at SSD of 711.2 mm (28 in). This is a drop of 23.9%, 37.2%, 30.8%, 29.3%, 26.7% and 21.6% for the PK6I, PK15I, PKBBI, PKWDI, R.45I-LP-AST and PK3I, respectively. For the 90º direction, the amplitude drop was 14.2%, 18.8%, 11.2%, 19.8%, 2.3% and 10.4% between the 50.8 mm (2 in) and 203.2 mm (8 in) SSD, respectively. The perimeter direction displays an amplitude drop of 11.6%, 26.4%, 4.9%, 10.1%, 6.3% and 3.0% between the 50.8 mm (2 in) and 965.2 mm (38 in).

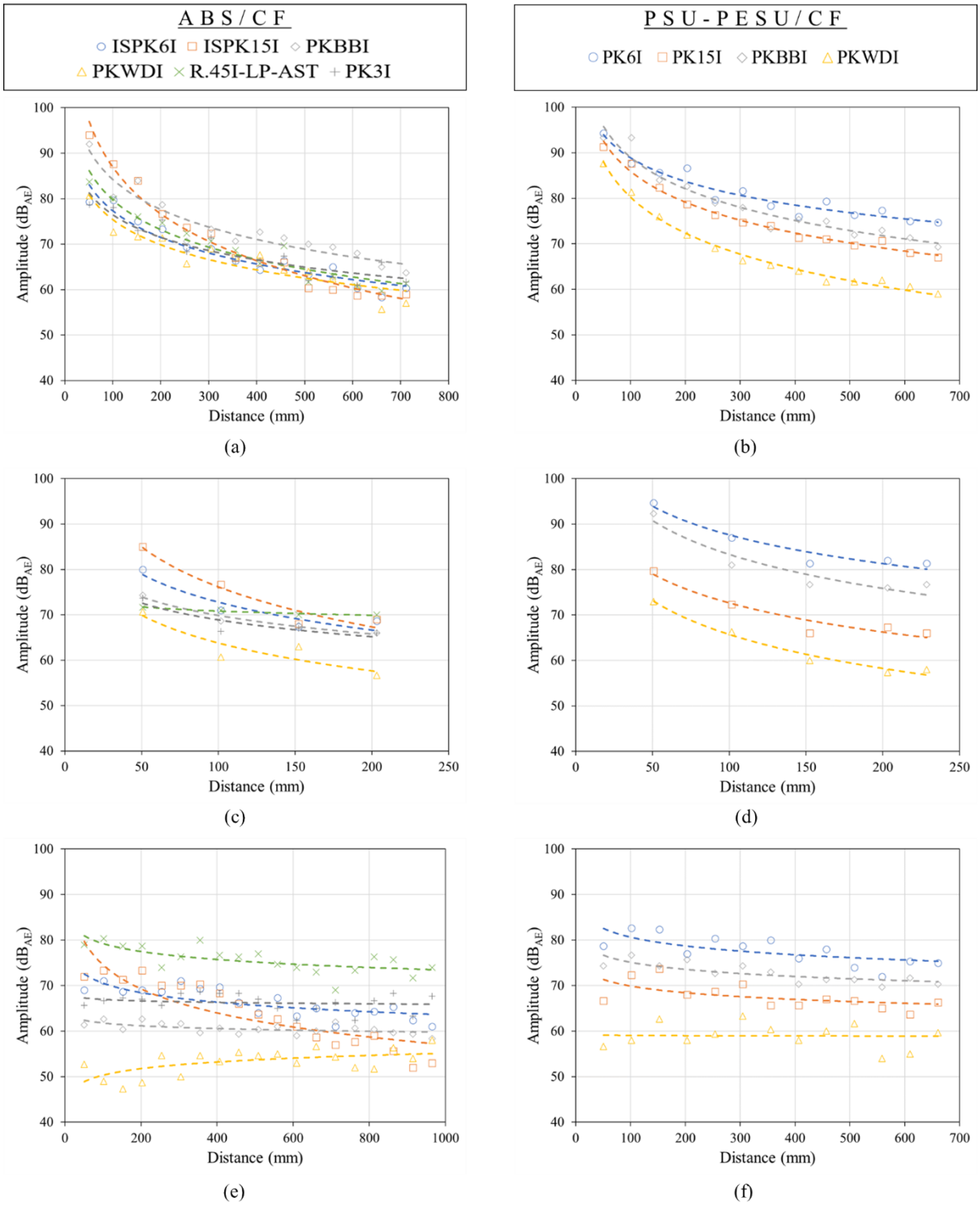

Figure 2: Attenuation results in the 0º direction, 90º direction, and perimeter direction for ABS/CF (a,c,d) and PSU-PESU/CF (b,d,f), respectively.

The process of sensor selection for any application is a delicate balance between sensitivity and analysis efforts. Typically, the higher the sensitivity of the sensors in the frequency of interest, the lower the number of sensors/channels which would be needed to cover the SHM for that application

and specimen. However, if there is any major source of noise in the sensitive frequency range of the sensors, then there will be a significant amount of time effort to comb through the data and distinguish which signals are relevant to keep and which ones are irrelevant and should be filtered before the analysis begins. In the case of polymer-based AM, it is expected to receive a lot of low frequency signals generated by the mechanical movements and the tamping of extruded material before they get cooled down. This would be irrelevant data if you are interested in the generation or progression of defects in the build and should be filtered out. The recommended approach would be to move to higher frequency sensors [32] [33]. Therefore, the R.45I-LP-AST and PK3I sensors were not used for further evaluation although they show acceptable sensitivity, given the attenuation curves in **Figure 2**.

The attenuation results for the PSU-PESU/CF are shown in **Figure 2**. The amplitude responses for the 0º direction orientations at 50.8 mm (2 in) SSD are 87.7 dB, 87.7 dB, 93.3 dB, and 81.33 dB and drop to 74.7 dB, 67.0 dB, 69.3 dB, and 59.0 dB at the 660.4 mm (26 in) SSD. This is 20.8%, 26.6%, 25.7%, and 32.7% drop in amplitude for the PK6I, PK15I, PKBBI, and PKWDI, respectively. For the 90º direction, the amplitude drop was 14.4%, 17.2%, 17.0%, and 20.5% between the 50.8 mm (2 in) and 228.6 mm (9 in) SSD, respectively. The perimeter direction displays an amplitude drop of 6.3%, 3.0%, 11.6%, and 26.4% between the 50.8 mm (2 in) and 660.4 mm (26 in).

Understanding the attenuation on these materials will assist in sensor selection and will provide a good understanding for the number of sensors required for a set inspection area. As it can be noticed from Figure 2, the study provided details on the amplitude response that can be captured for the tested material and corresponding failure mechanisms. There are three main factors that need to be balanced when selecting an optimal sensor for this application: (1) minimum attenuation decay, (2) maintaining a high response amplitude above a selected threshold to improve signal-to-noise ratio, and (3) selecting a frequency bandwidth to differentiate different event mechanisms. A sensor with high decay in detecting amplitude will be ranked lower due to its limitation to detect an excitation event over a long distance. A sensor showing minimum amplitude decay is ranked higher for sensor selection for its ability to detect acoustic signals over a long distance. Also, a frequency analysis is recommended to understand the frequency response of each sensor for the excitation type (i.e., crack initiation, crack propagation, etc.). The frequency analysis describes the frequency response, from the excitation source and material interaction, captured by a specific sensor.

Surface Roughness

The roughness of the printed surface was evaluated for ability to propagate the acoustic waveform, shown in **Figure 3**. PSU-PESU/CF was the print material used for this investigation. Three samples of 150 mm x 250 mm (6 in x 10 in) size where the surface roughness varied from the original print surface, a locally-milled region, and a completely-milled surface. Each milled specimen was machined to a depth of ~4 mm, removing the print ridges. The AE setup consisted of an alpha-15R sensor attached 25 mm (1 in) away from the edge, with DOW CORNING – high vacuum silicon grease. The alpha-15R sensor was selected to investigate the surface response at a 150 kHz sensor resonant frequency. On the other end of the sample, a PLB was performed 100 mm, 125 mm, and 150 mm away from the AE sensor to provide an amplitude response and a brief attenuation curve.

The amplitude response, shown in **Figure 3**, displays the original print surface resulted in the lowest amplitudes at all distances having an average of 80.1 dB. This can be related to the rough ridges the print process creates causing high scatter of the acoustic waveform. The locally-milled surface provided the highest average amplitude response of 86.3 dB. For the attenuation of each surface, the locally-milled surface provided minimum decay while the completely-milled surface had the most attenuation. When the surface is milled to the ~4 mm depth, this exposes the center of the print beads where the fiber orientation is random [34]. The surface wave caused by the PLB interact with the

random fiber orientation which causes higher attenuation. The original print surface has fiber alignment on the outer regions of the print bead. The surface waves can travel along the surface uninterrupted with the aligned fibers and results with moderate attenuation. This helps support the AM printed structure does not need to be completely machined flat for the application of AE monitoring, which aligns with current motivation to perform as little post-processing to the printed structure as possible. A reasonable local-milled flat surface for the AE sensor to attached to is a more realistic approach. Although, the original print surface provides sufficient amplitude and minimum signal attenuation, it is also reasonable to perform no post-processing step. Future investigation could assess a larger print structure to provide more data points for the attenuation curve. Also, a broad-band sensor would allow a frequency analysis to see which surface finish eliminates/contributes certain frequency spectrums.

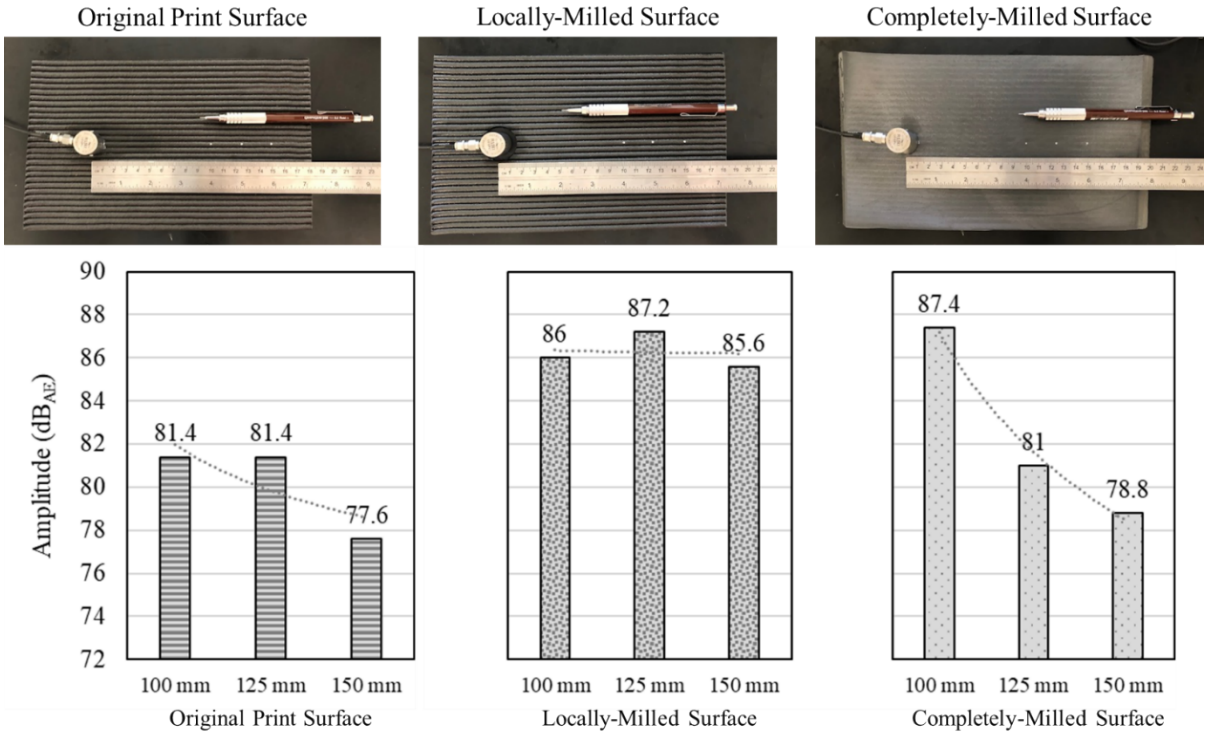

Figure 3: The amplitude response and attenuation curve for an original print surface, locally-milled surface, and completely-milled surface.

Attenuation of Large Printed Wall

To fully understand the acoustic decay properties of large printed structures, a 120 cm x 120 cm (4 ft x 4 ft) wall structure was constructed with ABS/CF material. This allows for AE amplitude measurements to be taken at greater distances and develop out the attenuation graphs. Three orientations were evaluated: 0º which is axial to the printed bead direction, 90º which is along the printer build direction and 90º direction to the bead orientation, and 45º which is in between. A broadband AE sensor was placed at the corner of the wall structure where the location was locally-milled for improved acoustic signature capture. Three PLB events were performed every 50 mm increments to build out the attenuation curves for each orientation. **Figure 4** displays the large printed structure and the associated experimental setup.

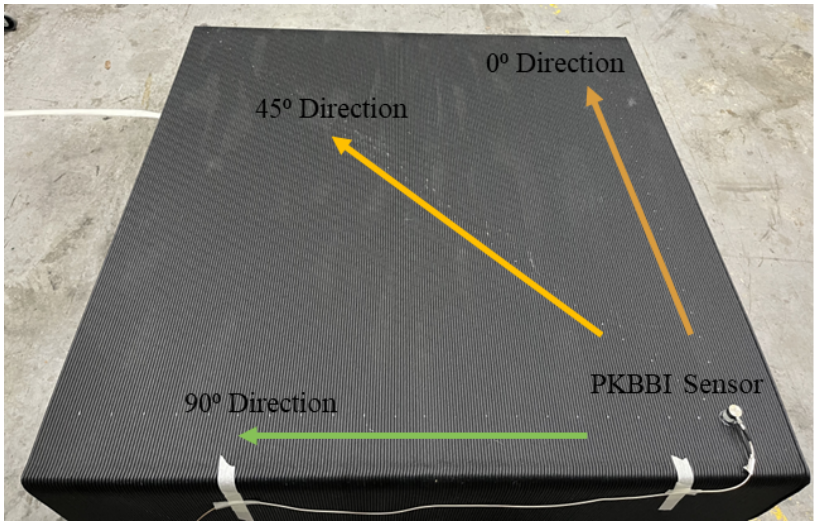

Figure 4: Printed wall structure for long distance attenuation study.

The large structure enabled testing at greater distances from the sensors. Figure 5 illustrates the attenuation curves for each orientation over extended distances. In the 0º direction, the amplitude showed a consistent decay along the entire length of the structure, yet it never dropped below the preset 40 dB threshold filter applied to mitigate background noise. In contrast, the 45º and 90º directions exhibited a sharp decline in signal response, crossing the 40 dB threshold at just 400 mm from the sensor, which is only one-third of the structure's total length. These findings highlight how the internal fiber orientations affect acoustic signal propagation. The 0º direction, with fibers aligned along the printed bead axis, facilitates wave propagation. Meanwhile, in the 45º and 90º directions, fibers are oriented transversely, significantly attenuating the signal. Additionally, the printed layer interfaces in these directions further impede wave propagation. This study provides a comprehensive mapping of anisotropic attenuation curves for large-scale printed structures and details the limitations regarding sensor placement distances.

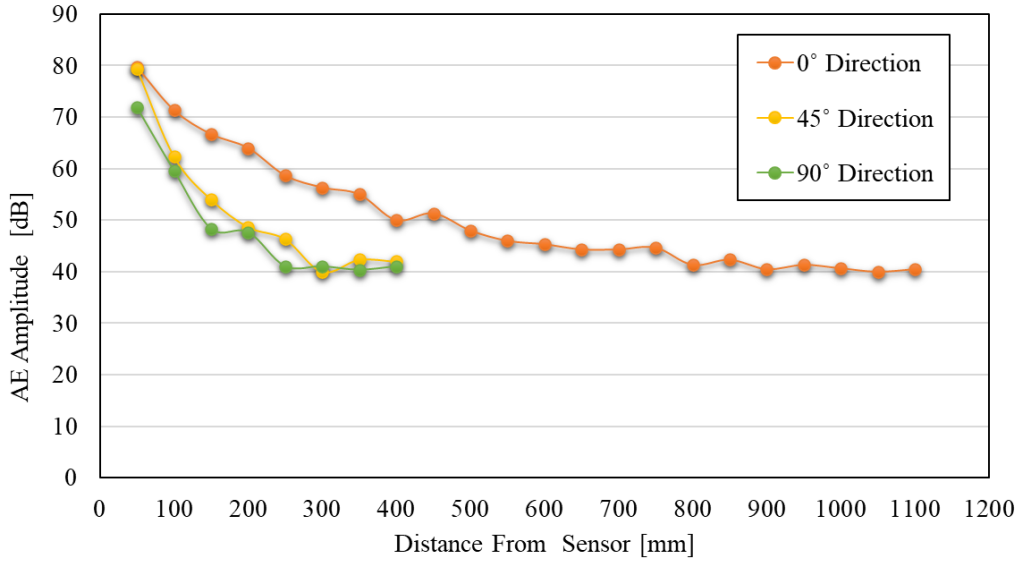

Figure 5: The attenuation curve of the large printed structure.

1.2.2 AE Background Noise Monitoring – Extruder

The background noise of the extruder was measured on a stand-alone system (Strangepress, Model-30) which has similar characteristics to the extruder used on the BAAM system, shown in **Figure 6**. There are three locations (Zone 1, 2, 3) where AE waveguides are screwed into the side of the extruder barrel housing. Each waveguide was coupled with a Nickel Anti-Seize (3M Loctite 77164) at each thread-point in the extruder. Before AE measurements, a thermal analysis using thermocouples and an infrared camera found the waveguide setup was thermally safe for the AE sensor staying well below the operating temperature of the sensors (120 ºC). Once the setup was determined to be safe for the AE sensors, PK15I sensors were attached to each waveguide and connected to the AE system (MISTRAS Micro-II Express). The extruder went through the following operations shown in **Table 2** while the AE setup monitored the amplitude response, average signal level (ASL), and frequency response to assess background noise. All AE results are measured across the time-domain which the extruder process takes place. A PLB is performed before and after the investigation to ensure each sensor does not lose sensitivity during the data acquisition. No sensitivity was lost during this investigation.

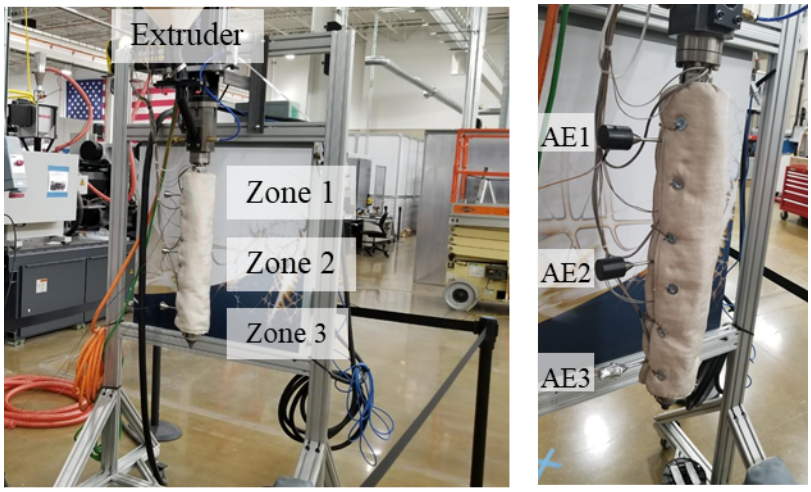

Figure 6: Extruder monitoring showing the; (a) stand-alone extruder barrel zones (1, 2, 3), and (b) where each waveguide is attached for the AE background monitoring.

Table 2: Extruder operation process and temperature settings.

Extruder Process	*Extruder Temperature Parameters*
1. PLB Before	Zone 1: 177 C
2. Control Noise (Extruder Off)	Zone 2: 220 C
3. Control Noise (Extruder On – Standby Cold)	Zone 3: 249 C
4. Heat up	
5. No Material (100 RPM)	
6. Material Load in Hopper	
7. Material Feed / Purge (250 RPM)	
8. Material Run [250, 500, 750, 1000, 1250, 1500 RPM, then 500 RPM (Purge)]	
9. Tamping Mechanism	
10. PLB After	

The AE was able to monitor the multiple routine processes the extruder would perform during printing. **Figure 7** displays the AE response during the extruder startup process including the system off as a control, the system on and cold, the system on and in heat-up cycle, and when material is loaded into the hopper. It can be seen, the ASL during system off and cold shows an average 20 dB amplitude of the noise with little deviation between Zone 1-3. This is the noise level of the surrounding manufacturing environment and AE system. When the extruder system is turned on, we see an increase in ASL to 33 – 34 dB with larger deviation between zones, around 7 dB. The heat-up cycle shows similar ASL response as the system on and cold, range of 32 – 34 dB, but with increase in fluctuation over time. There are also moments of scattered response, most likely due to the thermal expansion and frictional slippage events during heat-up. When material is loaded, there is a jump in ASL response to a maximum of 60 dB for Zone-1, the zone closest to the material hopper. When the amplitude response is viewed, we see an incremental order of each zone amplitude compared to its distance from the hopper. Zone-1 measures the highest amplitude at 72 dB, then a majority of Zone-2 response reaching 60 dB, and then a majority of Zone-3 response reaching 55 dB. Each amplitude response is associated to the ABS/CF pellet feedstock dropping into the barrel and colliding with the barrel walls.

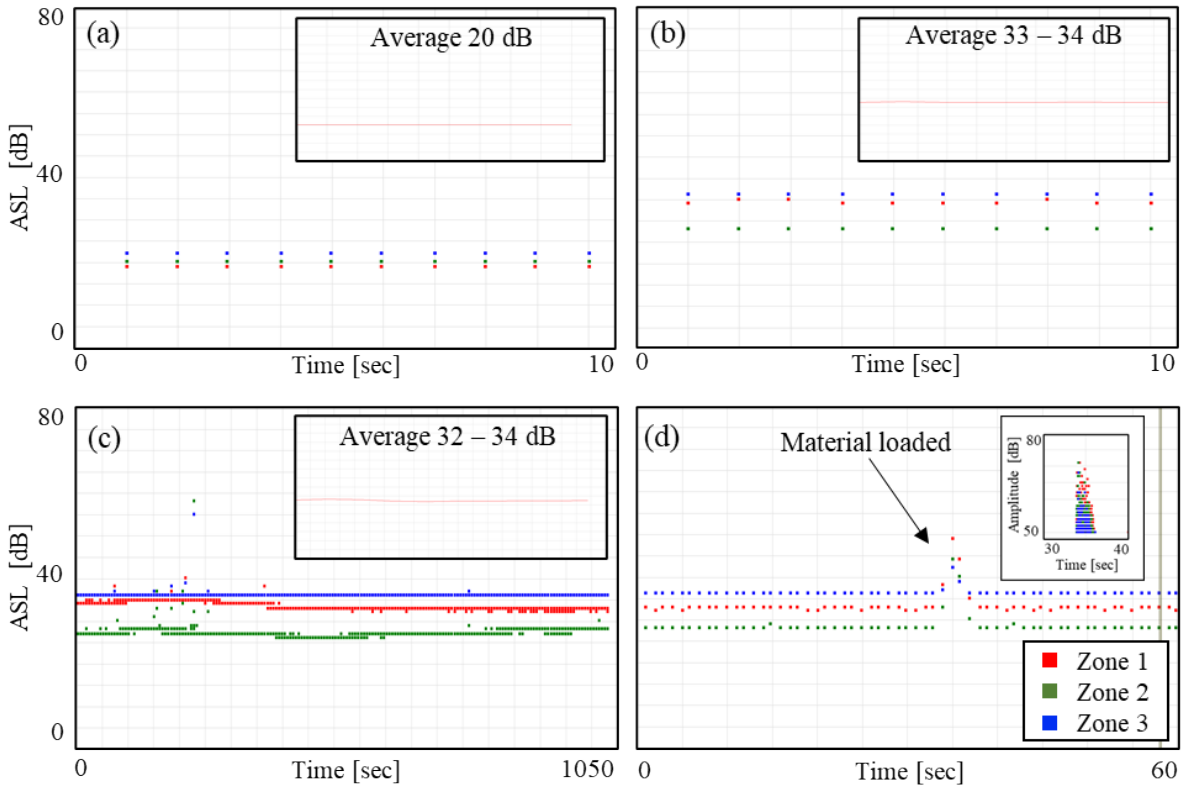

Figure 7: The ASL response for the extruder during; (a) the equipment in off position as a control, (b) the equipment turned on but with the extruder cold, (c) during the heat up of the extruder, and (d) when material was loaded into the hopper. For (a), (b), and (c), the average ASL response for all three zones is displayed with same time-domain. The material load amplitude response is shown within (d) reaching a maximum of 72 dB.

The process of purging the extruder was monitored with AE seen in **Figure 8**. The amplitude response shows the initial process of material traveling through the barrel within the first 60 seconds. Lower amplitude responses occur, with Zone-1 having the largest response, around 50-70 dB scatter. This is due to the un-melted pellets colliding at the top of the extruder barrel. There is this transition

where all zones experience an increase in amplitude response with range of 60 – 80 dB. It is suspected at this point, the extruder barrel is completely filled with material and has reached a thermal stability where there is a stable transition of the pellets from hard-to-molten stage. Zone-1 shows a higher response due to the un-melted pellets causing higher impacts, while Zone-3 shows a lower response due to the polymer being molten. The ASL response shows a similar trend and confirms. Shortly, the material is extruded out of the nozzle at 100 seconds with a similar amplitude response.

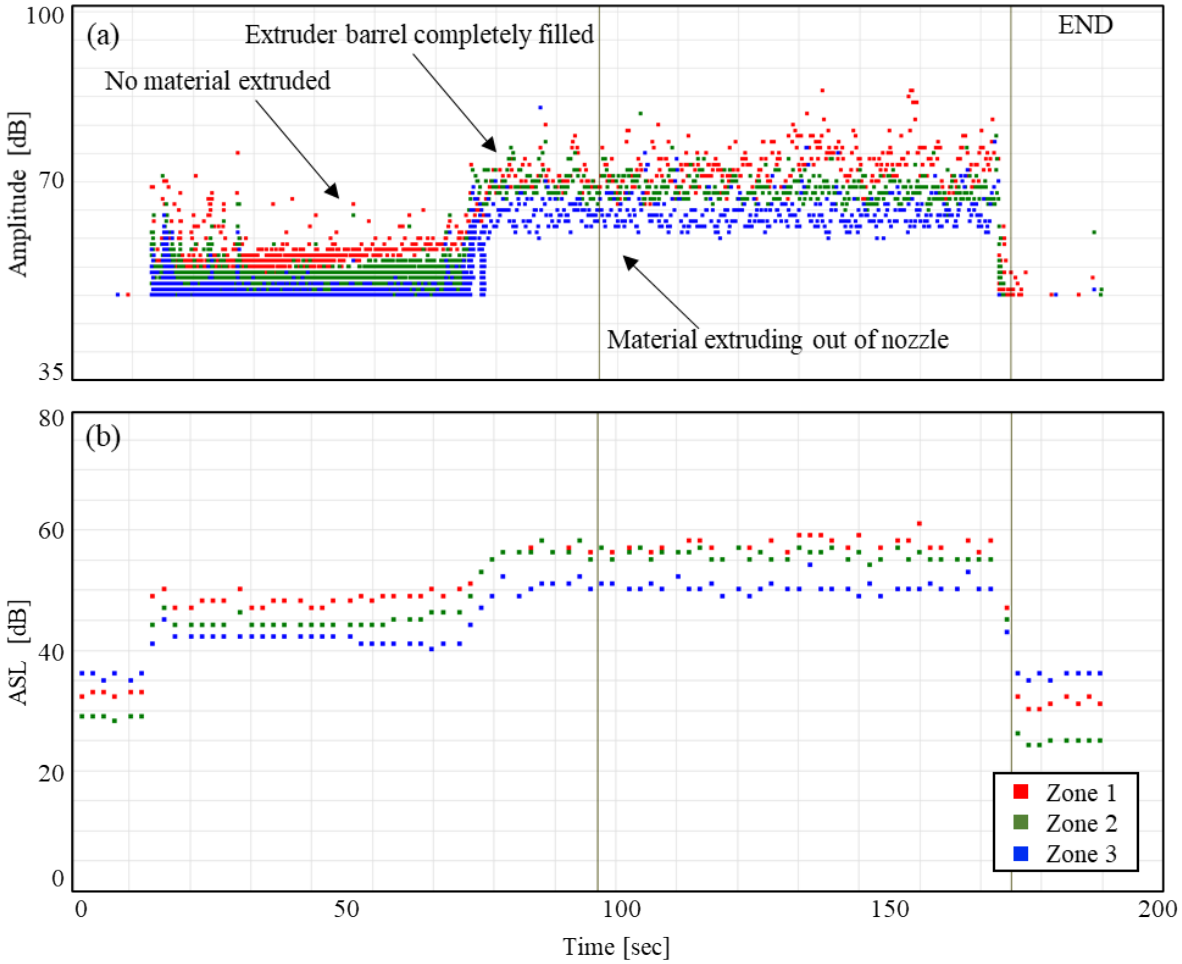

Figure 8: The extruder; (a) amplitude and (b) ASL response during material purge at 250 RPM. In increase in response is seen once material fully fills the barrel of the extruder and starts to extrude out of the nozzle.

The extruder went under a barrel screw speed investigation where the AE response is correlated to the increase screw rpm speeds, shown in **Figure 9**. It can be seen, at low screw speeds (250 rpm) there is a large deviation of amplitude response with a range of 60 – 85 dB. There is an increasing, converging trend where the deviation tightens up at 1500 rpm with majority of events at a range of 67 – 80 dB. The extruder was stopped between 1250 and 1500 rpm to see if the converging, increasing trend was truly associated to the extruder screw rotation. We see the trend continues as the extruder is turned on at 1500 rpm. The ASL response shows the same trend and confirms. A histogram of the amplitude response provides a clear distinction of when the extruder screw is on/off seen in **Figure 9(c)**. The two processes where the extruder screw is turned off display a low level of noise response, most likely due to the residual motion of the internal un-melted and molten polymer.

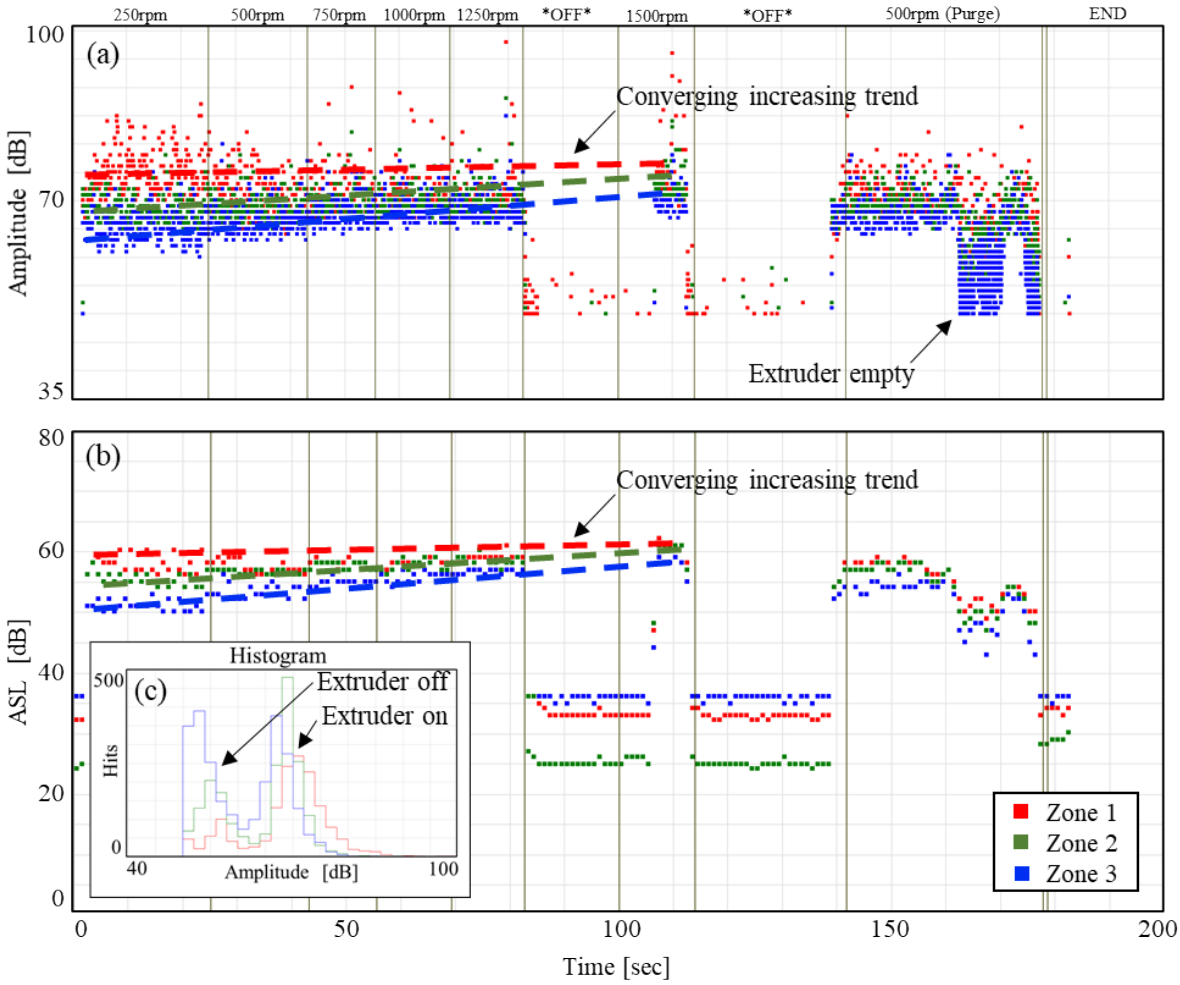

Figure 9: The extruder; (a) amplitude and (b) ASL response during the material run procedure. An increasing, converging trend for the amplitude and ASL response as the extruder's rpm increases. The distribution of hits and corresponding amplitudes are shown in the (c) histogram displaying a clear distinction when the extruder is on/off.

Further analysis was performed for the extruder screw speed investigation. The average amplitude of each zone shows an increasing, converging trend as the screw speed increases, displayed in **Figure 10(a)**. The peak-frequency response is captured for each screw speed, displayed in **Figure 10(b)**. It can be noticed the peak-frequency decreases as the screw speed increases, by a difference of ~10 kHz. Figure 10(c & d) provides additional support for the amplitudes and frequencies change within the frequency spectrum between 250 and 1500 rpm screw speeds. A reduction in higher frequency amplitudes is seen between the 250 and 1500 rpm within Zone-1. This may describe how the top of the extruder system resonates with greater amplitude at lower screw speeds. Now, there is an increase in amplitudes for the lower frequencies at Zone-3 when screw speeds are increased. This can be caused by larger dynamic displacements at the end of the extruder which acts as a large cantilever.

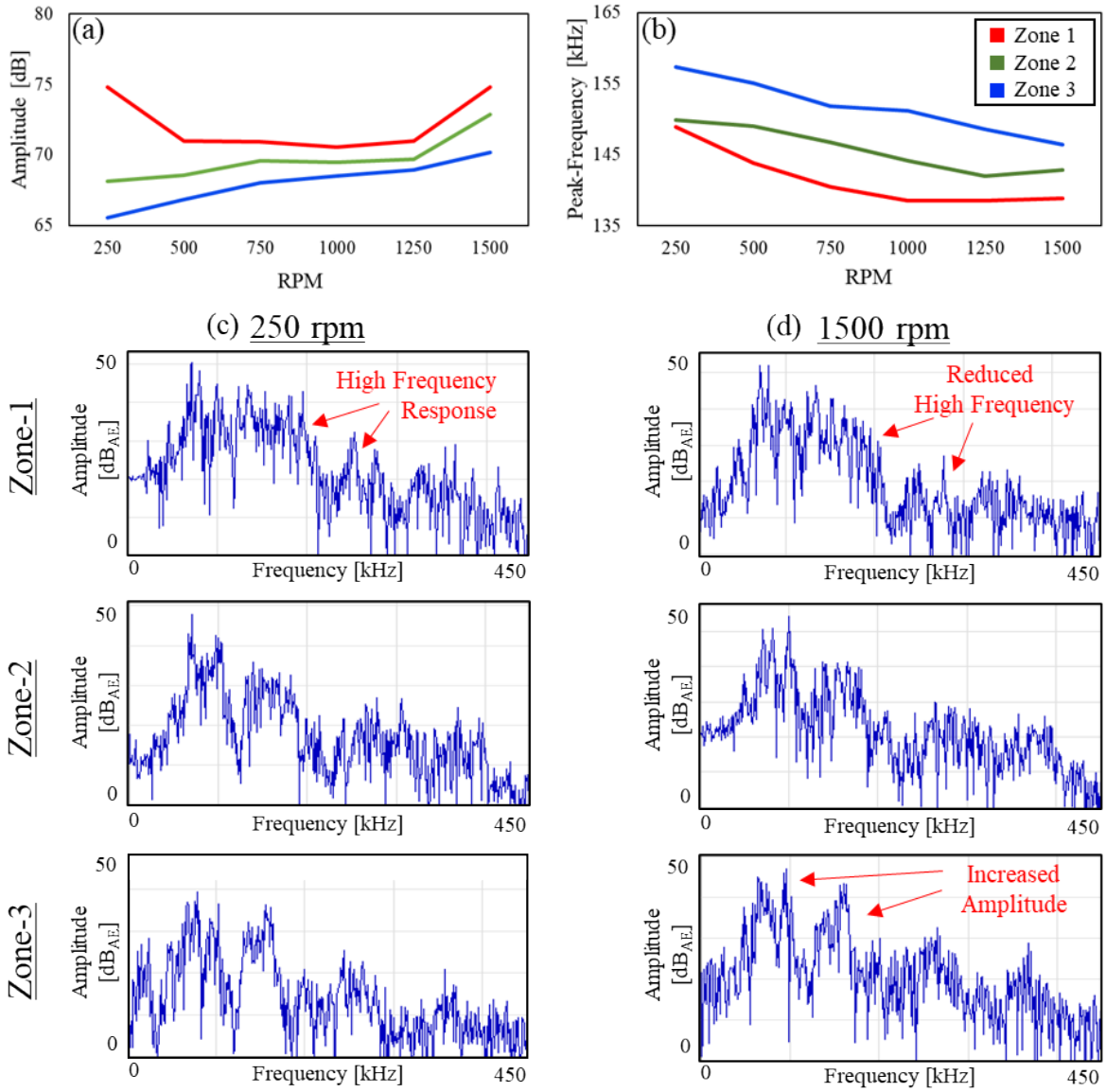

Figure 10: The amplitude and frequency response of the extruder during the material run process. The (a) average amplitude and (b) average peak-frequency response versus the screw speed. An example of the frequency response between (c) 250 rpm and (d) 1500 rpm for each zone.

The tamping mechanism running at 20 Hz was evaluated for noise. The variable frequency response can be seen in the waveform and frequency spectrum in **Figure 11**. Even with the tamping mechanism operating at a low frequency, higher frequency resonances are taking place and captured by the AE system. A 11.4 kHz low frequency response dominates the spectrum while there are multiple higher frequency resonances between 80 - 280 kHz. These frequencies can be suppressed by using a combination of narrowband and broadband filters. This will allow the detection of defect signals during the print process.

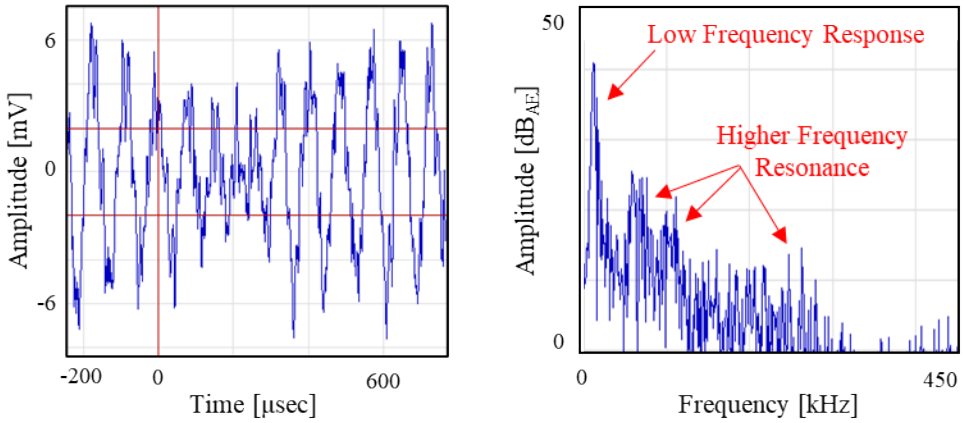

Figure 11: The noise response when the tamping mechanism is activated. A repetitive (a) waveform shows the multiple modes setup by the tamping oscillations. The (b) frequency response displays the low and high frequencies of the waveform.

Overall, there is little difference in the frequency response between low and high screw speeds other than the minor variances as described before. This can be identified as the background noise frequency response and can be used to filter out during the AM print process. All extruder processes displayed a higher noise response than expected. Although, the noise levels are still relatively lower than composite fiber and matrix damage. Typically, fiber and matrix cracks occur at a level of >80 dB. This is affected by sensor location and attenuation. Also, fiber breakage and matrix cracking frequency response typically occur in the high and mid-high frequencies, respectively.

1.2.3 AE Background Noise Monitoring – BAAM Gantry

The noise of the gantry system was monitored using AE. Two types of AE sensors were used, PK15I and PKWDI, placed on the extruder unit showed in **Figure 12(b)**. The PK15I sensor provides a focused response around 150 kHz with high signal-to-noise ratio and an operating frequency range of 80 to 450 kHz. Whereas, the PKWDI sensor is a broadband sensor which monitors a higher frequency range from 150 to 850 kHz with reduced sensitivity. These two options capture a full spectrum of frequency ranges. The BAAM gantry system monitored the X-, Y-, and Z-axis (both bed and extruder Z-motion). Each motion was performed as slow and rapid setting; 5 cm/s and 25 cm/s (2 in/s and 10 in/s), respectively. A PLB was performed before and after found no sensitivity loss occurred during this investigation.

Figure 12: The (a) large-scale BAAM system at ORNL-MDF has multiple sources noise for the gantry system. The AE sensors are attached as they would be during in-use, on the (b) extruder, to monitor all sources of noise.

The ASL response was collected during all gantry motions, shown in **Figure 13**. Each motion consisted of moving for 3 – 5 seconds at the respected rate (slow/rapid) then stopping to pause before moving again. A controlled measurement with no motion performed showed an averaged 22 dB response. All motions had an increased response of 30 dB noise level, an 8 dB increase from the control. The process with the highest fluctuation of ±0.5 dB was the Z-Extruder motion during rapid motion. All other gantry motion remained constant during each motion. This can be concluded the gantry background noise has a small range and low amplitude with minimum influence. A combination of using filtering and thresholds can eliminate the effect of the gantry noise. It was also noticed operator movement (walking) on the platform showed no increase in response from the controlled measurement.

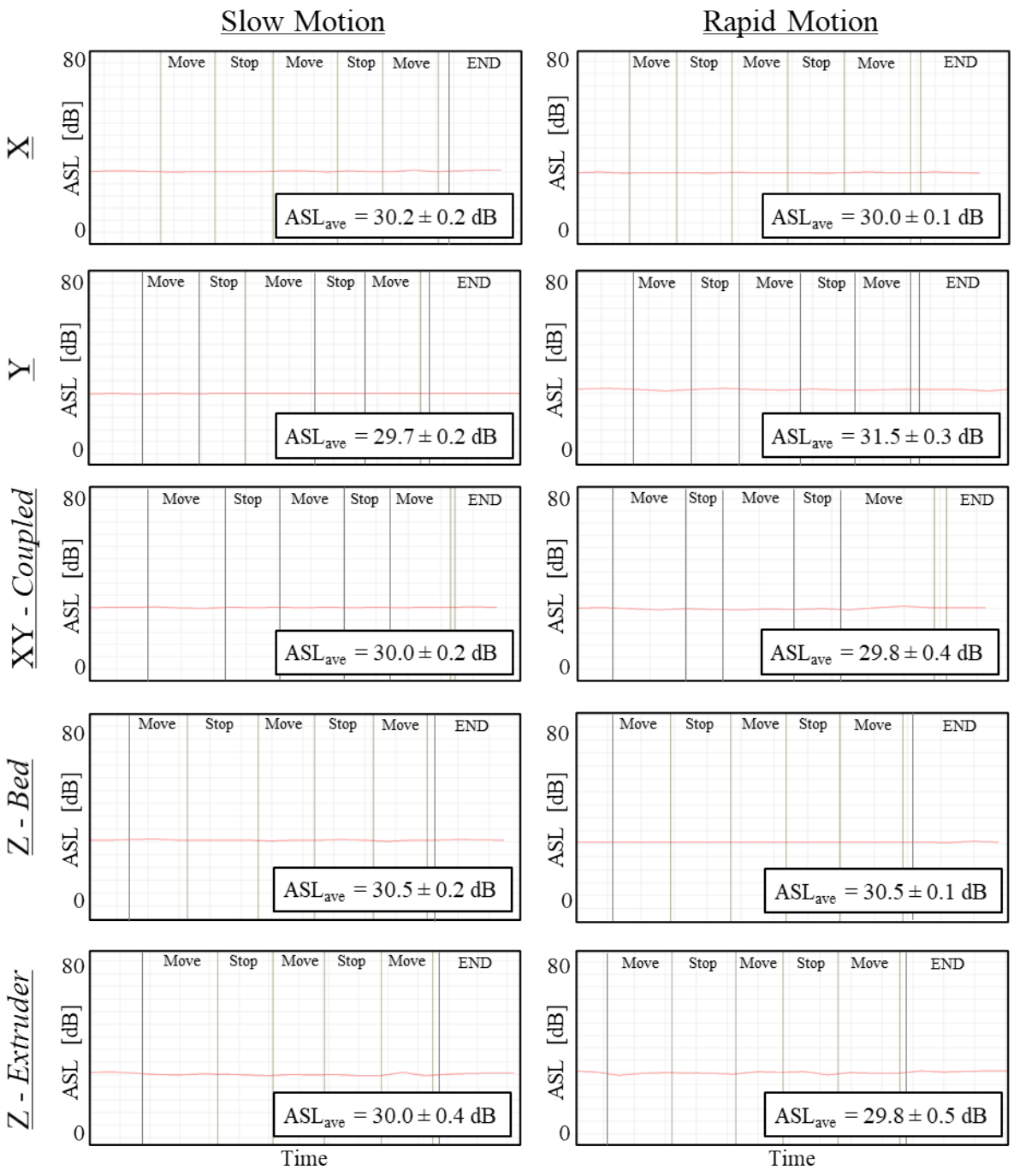

Figure 13: The ASL response for the BAAM gantry system. Noise levels were monitored for rapid and slow rate for the X, Y, XY-Coupled, Z-Bed, and Z-Extruder motions. All ASL are plotted across a time-domain, with non-relevant values but with the amount of time necessary for each process.

Each motion's waveform and frequency response were evaluated. **Figure 14** depicts the X-motion response as an example but represents all other motions. There were no noticeable differences between the slow and rapid speed. Both speeds have a low frequency response close to 0.5 kHz and higher frequency resonances range between 100 – 300 kHz with a center frequency of 225 kHz and 210 kHz for the slow and rapid speeds, respectively. There are a series of harmonics captured within the higher frequency bandwidth most likely associated with the gantry motors. As mentioned before, these noise responses can be eliminated with a series of filters to allow the capture of any defect anomalies during the print process.

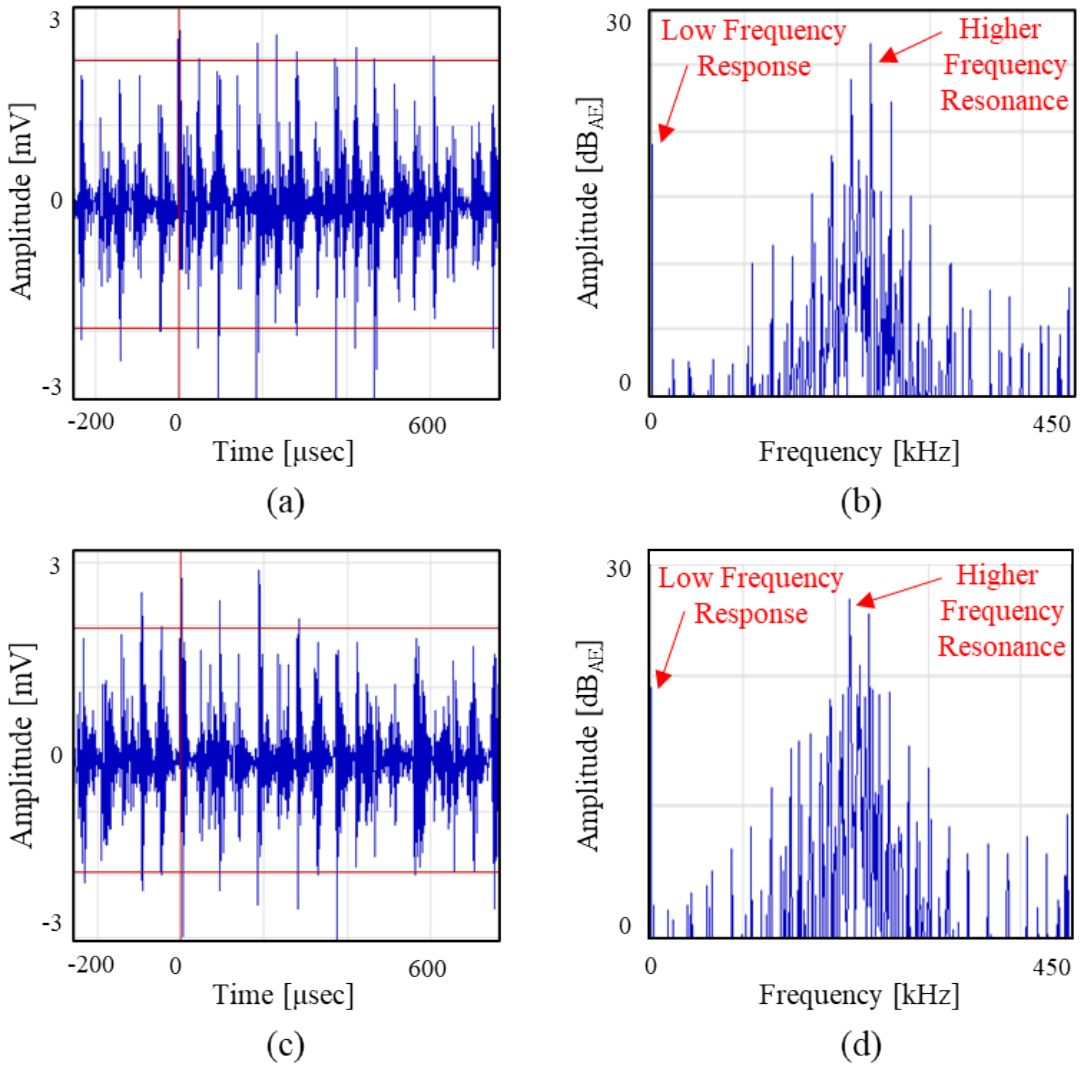

Figure 14: The waveform (a,c) and frequency spectrum (b,d) during slow (a,b) and rapid (c,d) motion, respectively, in the X-direction.

1.2.3 Sensor and System Specifications for Sensor Placement

Signal Signature and Frequency Analysis

The attenuation study performed in Section 1.2.1 displays the decay in amplitude response versus the distance in PLB is away from the sensor. Selecting sensors for structural health monitoring (SHM) involves balancing sensitivity with analysis efforts. This balance is crucial for effective SHM. Higher sensitivity sensors in the target frequency range reduce the number of sensors needed for comprehensive monitoring. Consequently, higher frequency sensors are recommended, which led to the discontinuation of the R.45I-LP-AST and PK3I sensors in this study (**Figure 2**).

Understanding attenuation in the materials being monitored assists in sensor selection and determining the number of sensors required for a specific inspection area. Three main factors influence optimal sensor selection: (1) minimal attenuation decay, (2) maintaining a high response amplitude above a selected threshold to improve signal-to-noise ratio, and (3) available frequency bandwidth to differentiate various event mechanisms. Sensors with high attenuation decay are less effective over long distances, while those with minimal decay are preferred for their ability to detect acoustic signals over extended ranges. Frequency analysis is also crucial for understanding each sensor's response to different excitation types (e.g., crack initiation and propagation).

Frequency analysis was conducted using the Fast Fourier Transform (FFT) on waveforms detected by the PKBBI and PKWDI sensors at a 15.2 cm (6 in) PLB excitation location along the 0-degree orientation. Broadband sensors were used due to their uniform frequency response without bias, unlike resonant sensors (e.g., PK15I), which have a narrow response bandwidth. **Figure 15** and **Figure 16** show the time-domain waveforms of excitation events and their corresponding FFT responses in ABS/CF and PPSU-PESU/CF printed hexagons, respectively. Table 3 lists the measured frequency ranges and peak frequency responses from the FFT analysis, compared to the sensors' operating frequency ranges and resonance specifications.

For ABS/CF, the PKWDI sensor best characterized the print material due to its broad frequency range and multiple frequency peaks. The PKBBI sensor showed a lower amplitude response with fewer resonance peaks. In the PPSU-PESU/CF analysis, the PKWDI sensor also recorded higher signal amplitude, similar to the ABS/CF results. The PKWDI sensor displayed the highest power contribution across a broad frequency range, useful for identifying different damaging mechanisms at specific frequencies. The PKBBI and PKWDI sensors have operating ranges up to 600 kHz and 850 kHz, respectively. However, no signal response was detected above ~350 kHz for both materials, likely due to high attenuation from the internal microstructure, including reinforced carbon fiber and potential internal anomalies like voids.

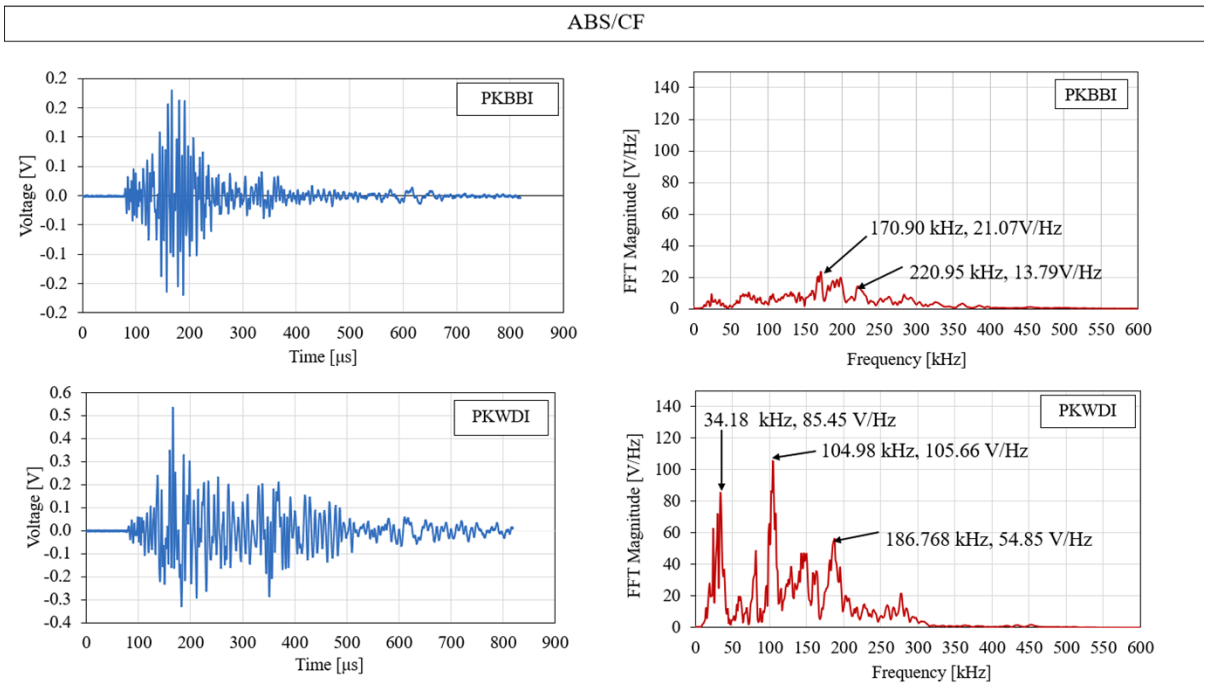

Figure 15: The waveform and FFT frequency response comparing different sensors at a set 6-in distance of the 0-degree attenuation curve for ABS/CF material using the PKBBI and PKWDI sensors.

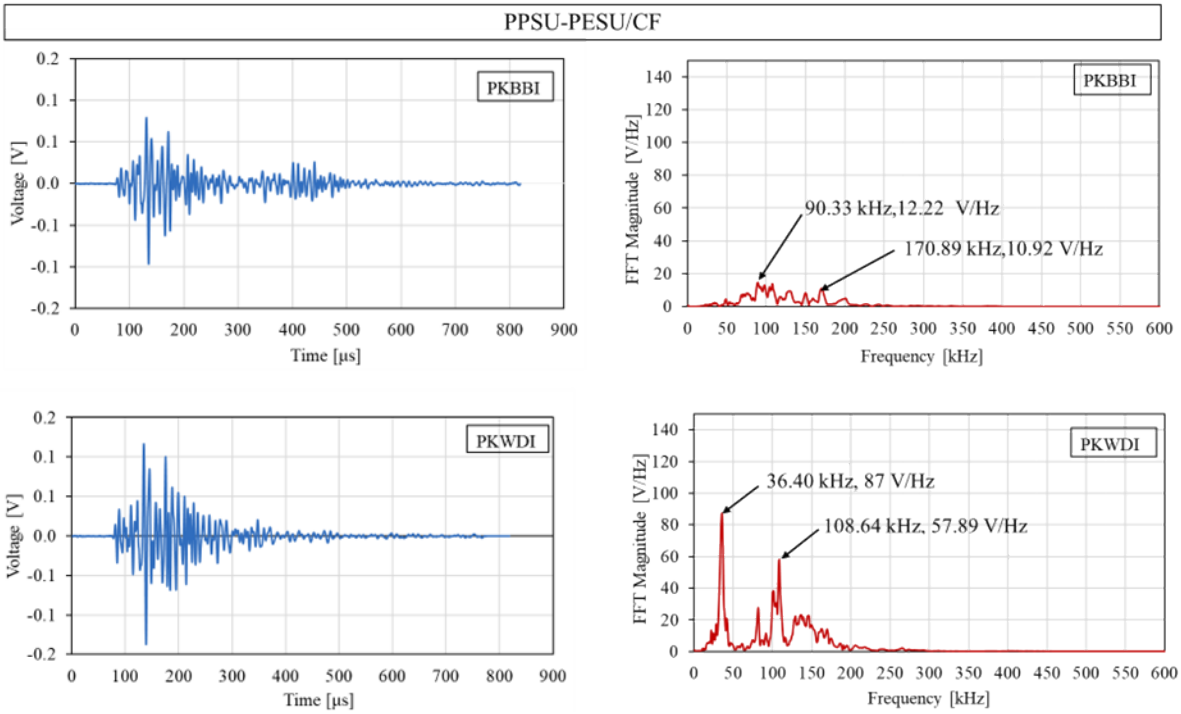

Figure 16: The waveform and FFT frequency response comparing different sensors at a set 6-in distance of the 0-degree attenuation curve for PPSU-PESU/CF material using the PKBBI and PKWDI sensors.

AE Sensor Placement

Building on the wave attenuation findings from section 1.2.1, the optimal placement of sensors will be investigated. This task will also identify the number of AE sensors required to effectively monitor a large printed structure. For taller prints, acoustic energy is significantly attenuated before it reaches sensors placed on the printing platform, necessitating the potential relocation of sensors to the printed part itself.

The attenuation study also determines sensor spacing and the number required for comprehensive inspection coverage. Each sensor's attenuation curve fits a logarithmic decay model (**Equation 1**),

$$A_{dB} = \alpha \ln(d_s) + \beta$$

Equation 1

where A_{dB} is the amplitude response, d_s is the distance from the PLB excitation source to the sensor, β is the amplitude intersect, and the α is the attenuation coefficient. Equation 3 is rearranged to calculate the radial response distance of the sensor (**Equation 2**),

$$d_s = e^{\frac{1}{\alpha} A_{dB} - \beta}$$

Equation 2

A threshold amplitude of 55 dB is set for sensor spacing calculations using **Equation 2**. This threshold maximizes signal amplitude while minimizing noise interference. The AE system is set to capture signals above a 45 dB threshold to distinguish noise from valid excitation amplitudes. Noise investigation is crucial to set an appropriate threshold. Sensor distances are doubled to determine the spacing between sensors, outlined in **Figure 17**. **Figure 18** provides results for ABS/CF and PPSU-PESU/CF sensor spacing in different orientations and sensor types. For ABS/CF, the PKBBI sensor achieves the longest spacing at 432 cm and 249 cm for 0-degree and 90-degree orientations, respectively. Generally, sensor spacing tends to be larger in the 0-degree orientation due to carbon fiber alignment and polymer crystallinity effects [27]. In contrast, the 90-degree orientation experiences higher attenuation from bead interfacial interactions and 90º direction fiber orientations, resulting in shorter sensor spacing. This trend aligns with observations from the wave propagation study discussed earlier. Similarly, PPSU-PESU/CF material shows larger sensor spacing in the 0-degree orientation compared to the 90-degree orientation. The PK6I sensor achieves the maximum spacing with 1833 cm and 703 cm for 0-degree and 90-degree orientations, respectively, whereas the PKWDI sensor provides the smallest spacing at 183 cm and 53 cm for the same orientations.

Comparing the two materials, PPSU-PESU/CF generally exhibits larger sensor spacing across most sensor types compared to ABS/CF. This difference is likely due to the higher carbon fiber content (25% versus 20% in ABS/CF), resulting in increased material stiffness [35, 36] and reduced damping [37]. Lower damping correlates with reduced attenuation, allowing for greater sensor spacing.

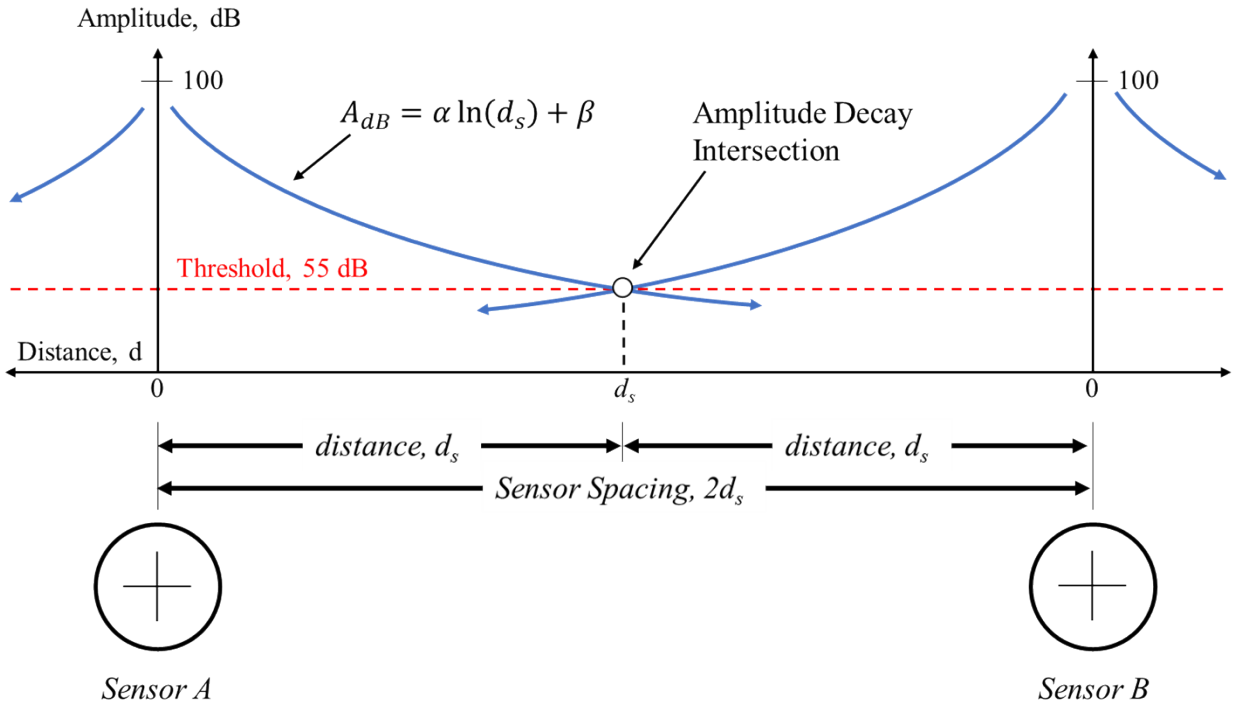

Figure 17: Schematic of how the attenuation curve determines the sensor spacing based off a set threshold and where the attenuation curves intersect at the amplitude decay intersection point.

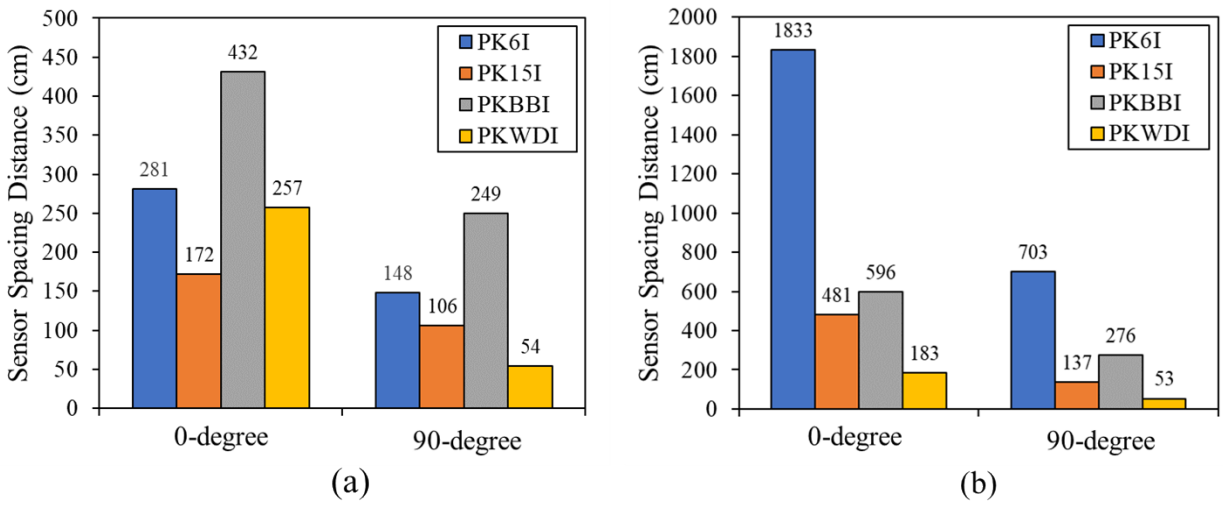

Figure 18: Sensor spacing calculation for 0-degree and 90-degree orientation; (a) ABS/CF and (b) PPSU-PESU/CF.

Simulated Sensor Spacing Analysis

Based on these findings, sensor spacing calculations can be performed for a simulated large-scale AM printed wall with dimensions of 6.1 meters in length and 1.5 meters in height (20 feet by 5 feet), which matches the full build size of the BAAM machine at ORNL-MDF using a single-bead

extrusion method. **Figure 19** illustrates the schematic visualization of various sensor distributions and spacing distances for both ABS/CF and PPSU-PESU/CF. The sensor placement is determined by the 0-degree and 90-degree sensor distance measurements. Results show minimal decay in the perimeter attenuation, indicating that only 1-2 sensors are needed to monitor waveforms across the same area. Future research could investigate a nesting technique for sensor distribution that considers all attenuation orientations, optimizing sensor placement through staggered arrangements [38].

For ABS/CF, the PKWDI sensor would require nine sensors to cover the 6.1 m x 1.5 m wall, whereas the PKBBI sensor would only need two sensors for the same coverage. The PK6I and PK15I sensors would require six and eight sensors, respectively. For PPSU-PESU/CF material, the PKWDI sensor would necessitate twelve sensors. In comparison, the PK15I sensor would need four sensors, while the PKBBI would need only two. The PK6I sensor would require just one sensor for full coverage, making it the most efficient option.

This sensor placement analysis is critical for determining the number of sensors required for comprehensive monitoring and understanding the financial implications of full-scale coverage. It's important to note that this study uses simple geometry to establish the fundamental principles of applying AE to large-scale polymer AM. Additional research is needed to fully understand the impact on more complex structures, including variations in wall thickness, different internal infill patterns, and overall intricate 3D geometries.

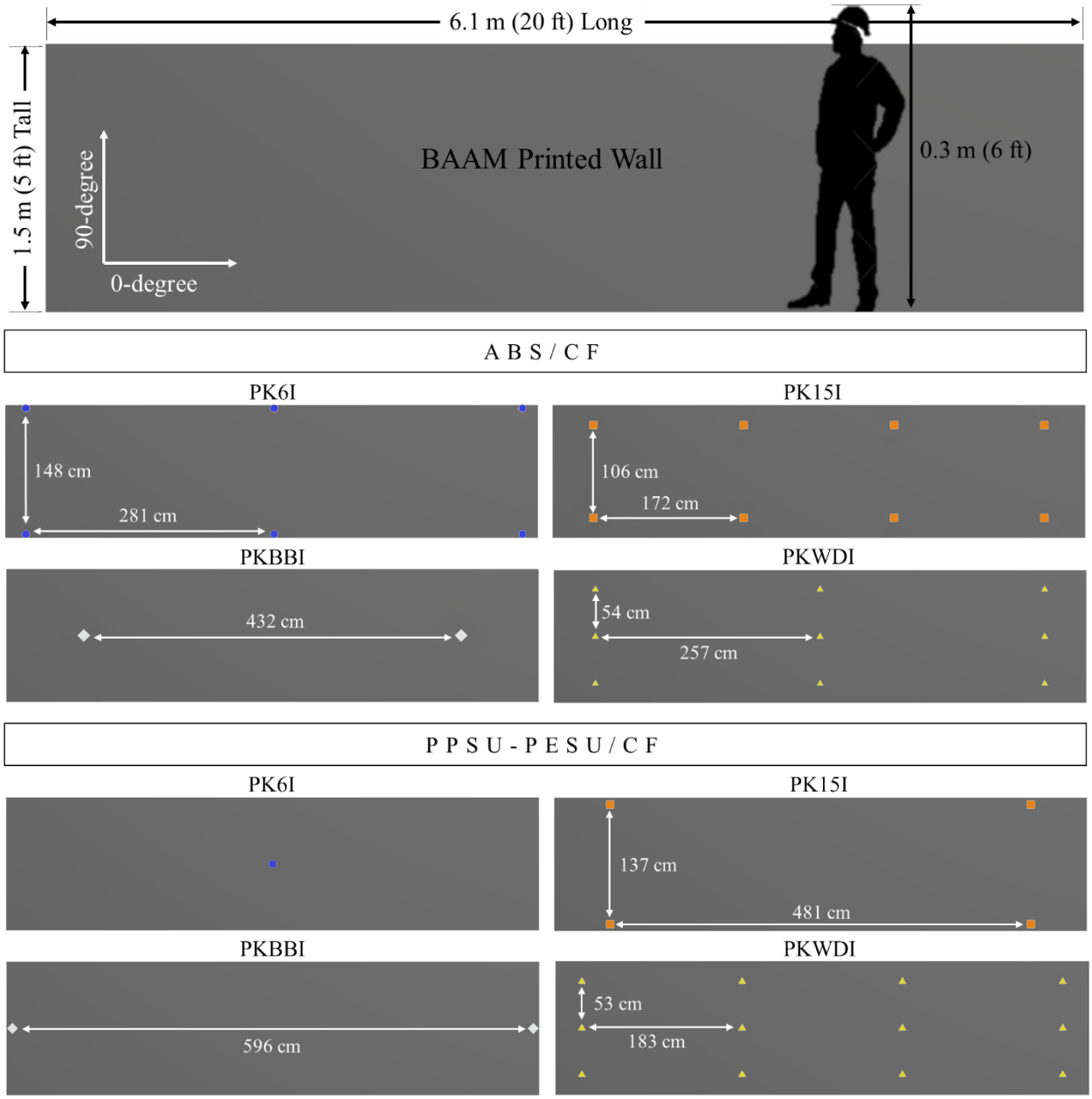

Figure 19: Schematic visualization for different sensors distribution and spacing distances for a large AM printed wall using ABS/CF and PPSU-PESU/CF.

Sensor Selection

The next step is to select sensors and strategize sensor implementation that will best monitor large scale printing. **Table 3** assesses the capabilities of various sensors for different material types by comparing their frequency response ranges, the number of sensors needed, and relative costs. Sensors with a broadband frequency response can detect a wide range of events but with lower sensitivity, while narrowband sensors are highly sensitive but may miss events outside their specific frequency range. The number of sensors required is based on a simulated large-scale printed wall, providing a comparative understanding of different sensor types. The cost analysis includes the AE system, per-channel cost, sensor cost, and the time needed for sensor installation and signal analysis.

The optimal sensor selection for each print material is discussed, emphasizing the possible need for multiple sensor types to cover a full range of excitations. For ABS/CF material, the PKBBI sensor is recommended for initial monitoring due to its broadband capabilities and minimal sensor requirement, allowing quick setup and comprehensive event capture. The PK6I sensor offers similar coverage with better low-frequency response but at a higher cost due to more sensors needed. After initial data collection, the PK15I sensor, with its narrowband around 150 kHz and some broadband response, is suitable for more focused monitoring, despite higher costs due to more sensors and increased analysis time. The PKWDI sensor, though having the broadest frequency response at 850 kHz, requires many sensors due to signal attenuation, leading to higher costs. The same recommendations apply to PPSU-PESU/CF, with the exception that fewer PK15I sensors are needed, reducing costs.

This sensor selection is based on simple geometry and a simulated demonstration. More complex geometries will require further investigation to fully understand attenuation responses. However, this study provides foundational steps that can be expanded for various applications.

Table 3: Sensor assessment for AE monitoring of ABS/CF and PPSU-PESU/CF print material for large-scale AM process.

Material	***Sensors***	***Frequency Response [Broad / Narrow]***	***Number of Sensors***	***Relative Cost [$]***
***ABS*/CF**	**ISPK6I**	Broad	6	$$
	ISPK15I	Narrow	8	$$$
	PKBBI	Broad	2	$
	PKWDI	Narrow	9	$$$
PPSU-PESU/CF	**ISPK6I**	Broad	1	$
	ISPK15I	Narrow	4	$$
	PKBBI	Broad	2	$
	PKWDI	Narrow	12	$$$

2.2.4 Validation Through Destructive Methods and Other NDT Techniques

The AM structure was printed using the Big Area Additive Manufacturing (BAAM) system at the Oak Ridge National Laboratory – Manufacturing Demonstration Facility (ORNL-MDF). This system can extrude at 45.4 kg/hr (100 lb/hr) and has a build envelope of 6.1 m x 2.4 m x 1.8 m (20 ft x 8 ft x 6 ft). The print material used was a polysulfone-polyethersulfone blend (PSU-PESU) reinforced with 25% carbon fiber (PSU-PESU/CF), specifically for a tooling application. After printing, the structure cooled at ambient temperature (73 °F), during which two large cracks formed due to thermal residual stresses from suboptimal printing conditions. These cracks, labeled as Crack 1 and Crack 2, measured between 40 to 46 cm in length (see **Figure 20**), with potential longer lengths where layers were in contact but not visible to the naked eye.

To assess crack propagation, the structure underwent a thermal cycle aimed at furthering crack

growth and evaluating the AE system's capability to detect and quantify this growth. Monitoring was conducted using a MISTRAS Group, Inc. Micro-II Digital AE system equipped with PK6I AE sensors. Eight AE sensors and three K-type thermocouples were installed on the structure to monitor the cracks and temperature changes, respectively (as shown in Figure 1). The AE sensors were divided into two groups: Group 1 (S1-S5) monitored Crack 1, while Group 2 (S6-S8) monitored Crack 2. Temperature measurements were recorded using a National Instruments DAQ system with an NI-9217 card. The structure was placed in a walk-in oven (GRIEVE TB-500) fitted with slip pads to minimize frictional noise and accommodate thermal expansion (see **Figure 21**).

The thermal cycle procedure, detailed in Table 1 and Figure 3, involved ramping the oven to 45 °C for a two-hour dwell, followed by a ramp to 75 °C for another two-hour dwell, before cooling back to room temperature. Pencil lead breaks (PLB) were performed before and after the test to verify the sensitivity of each sensor.

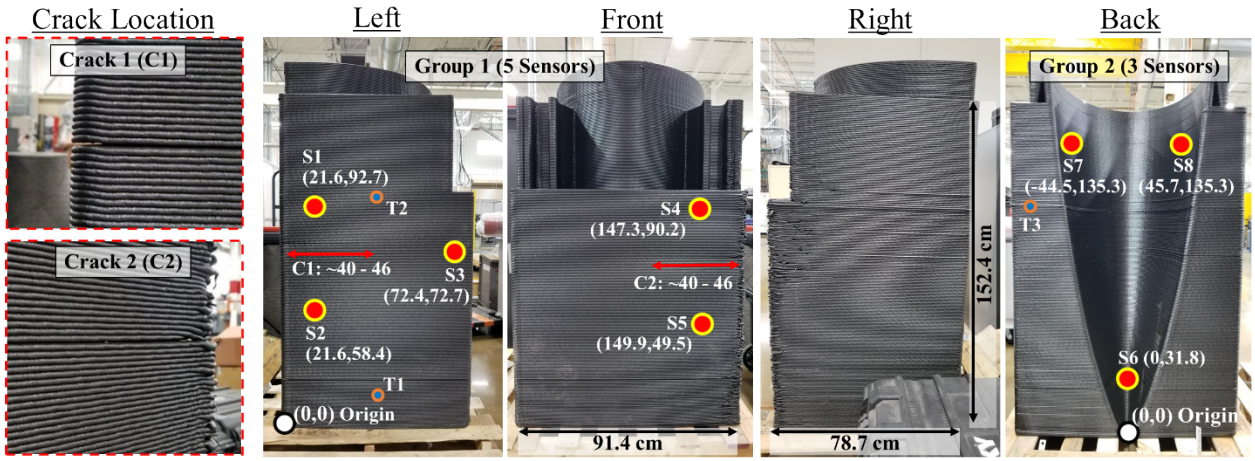

Figure 20: Large AM structure with pre-existing crack locations (C1 & C2) measuring 40 - 46 cm in length for each. Associated AE sensor locations (Group 1 and 2) to monitor crack growth in corresponding locations. Thermocouples (T1-T3) monitor temperature. Units in cm.

Figure 21: Thermal cycle setup with GRIEVE walk-in oven, thermocouple DAQ system, and the AE system. The AM Structure was placed on smooth slip pads to allow thermal expansion and reduce frictional noise.

During the heat cycle of the printed structure, multiple AE events were recorded and analyzed. **Figure 22** illustrates these events alongside the structure's temperature over time. Event 1 occurred shortly after reaching 35 °C, while Event 2 was detected after reaching 63 °C during the second ramp-up. Event 3 occurred around 3.5 hours into the cooling stage when the structure's temperature was at 64 °F (~18 °C). It's noted that this temperature correlates with layer separation for this specific print material and structure. The amplitudes for Event 1, 2, and 3 were 99 dB, 90 dB, and 96 dB, respectively. Other events were captured but identified as noise due to their low amplitude and waveform characteristics.

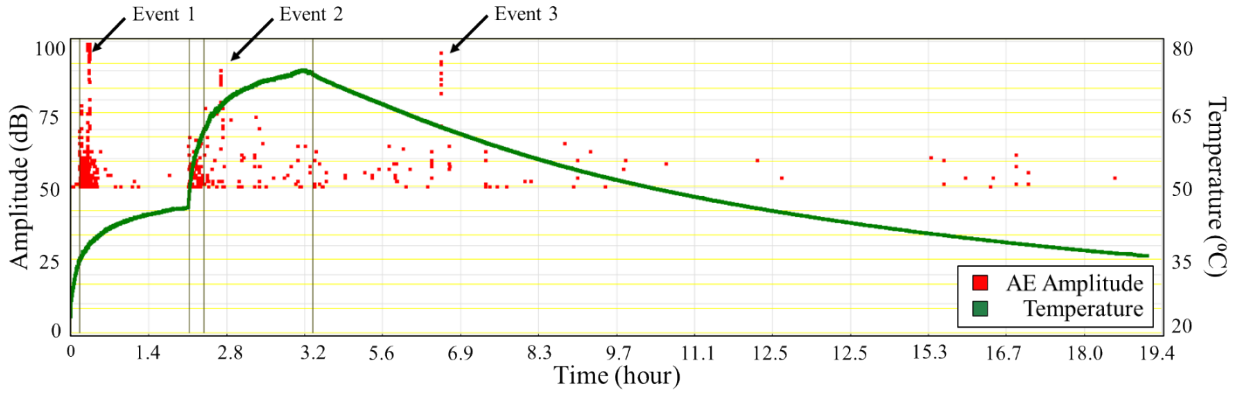

Figure 22: AE Amplitude vs Time with temperature parametric during the heat cycle. Events 1, 2, and 3 correlating to crack propagation/nucleation on the AM structure.

Figure 23 provides waveforms and spectrum analyses for Events 1, 2, and 3. Events 1 and 3 exhibited a broad frequency response from 0 kHz to 220 kHz, including higher frequencies above 150 kHz, indicative of fiber breakage. Event 2 showed a mid-frequency response up to 125 kHz, suggesting delamination or interfacial debonding. These frequency characteristics align with typical behaviors observed in polymer composites, where high frequencies relate to fiber breakage, mid-frequencies to delamination, and low frequencies to matrix cracking in traditional laminates.

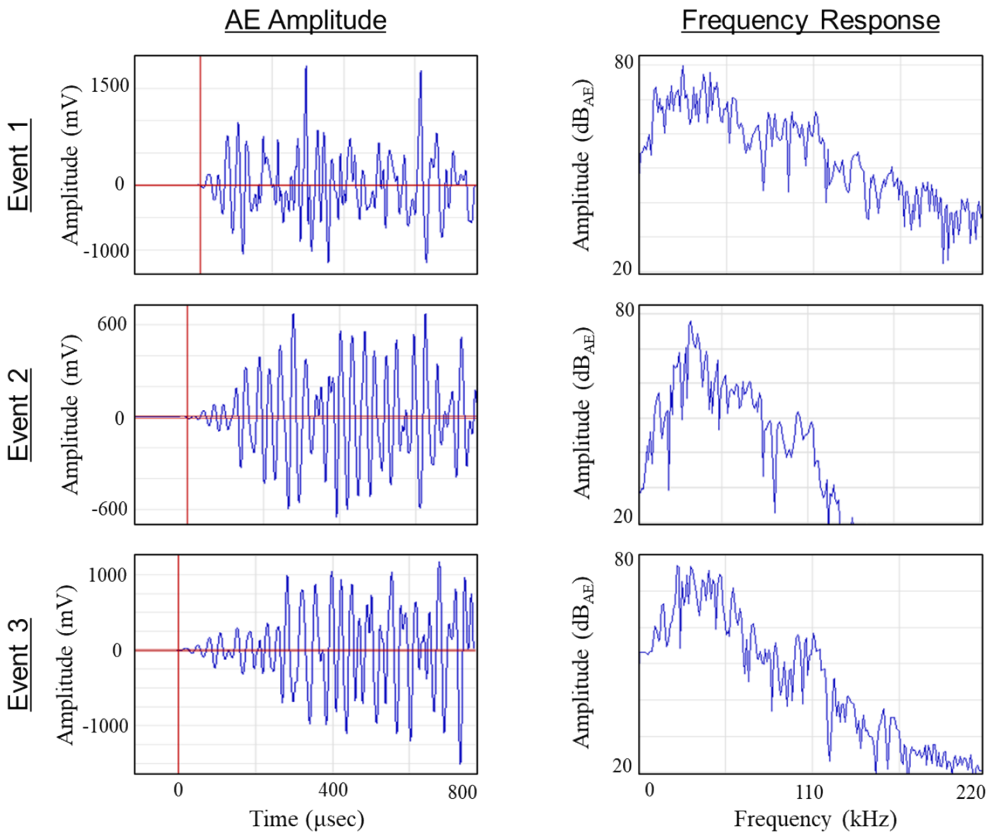

Figure 23: The AE amplitude and frequency response for Events 1, 2 and 3.

AE technology utilizes a 2D planar array of sensors to pinpoint event locations through time difference calculations (Δt), leveraging known acoustic velocities of materials. For the PSU-PESU/CF printed structure, which exhibits anisotropic acoustic properties, velocities along and 90º direction to the print bead direction are 3220 m/s and 1670 m/s, respectively. These values were inputted into AEwin software along with the structure's geometry and sensor positions to determine event locations related to crack growth, as shown in **Figure 24**.

Event 1 and 2 within Group 1 corresponded to the continuation of Crack 1 (C1) with XY coordinates at approximately 59.9 cm, 73.8 cm and 50.9 cm, 76.7 cm, respectively. Crack 1 initially measured between 40 cm to 46 cm in length (X direction) and appears to have extended to approximately 50 cm to 60 cm. Event 1 and 2 captured the ongoing layer separation associated with Crack 1. In Group 2, located within the conical geometry of the AM structure, Event 3 was recorded at coordinates -39.1 cm, 125.9 cm. No preexisting crack was visually observed in this area before the thermal cycle.

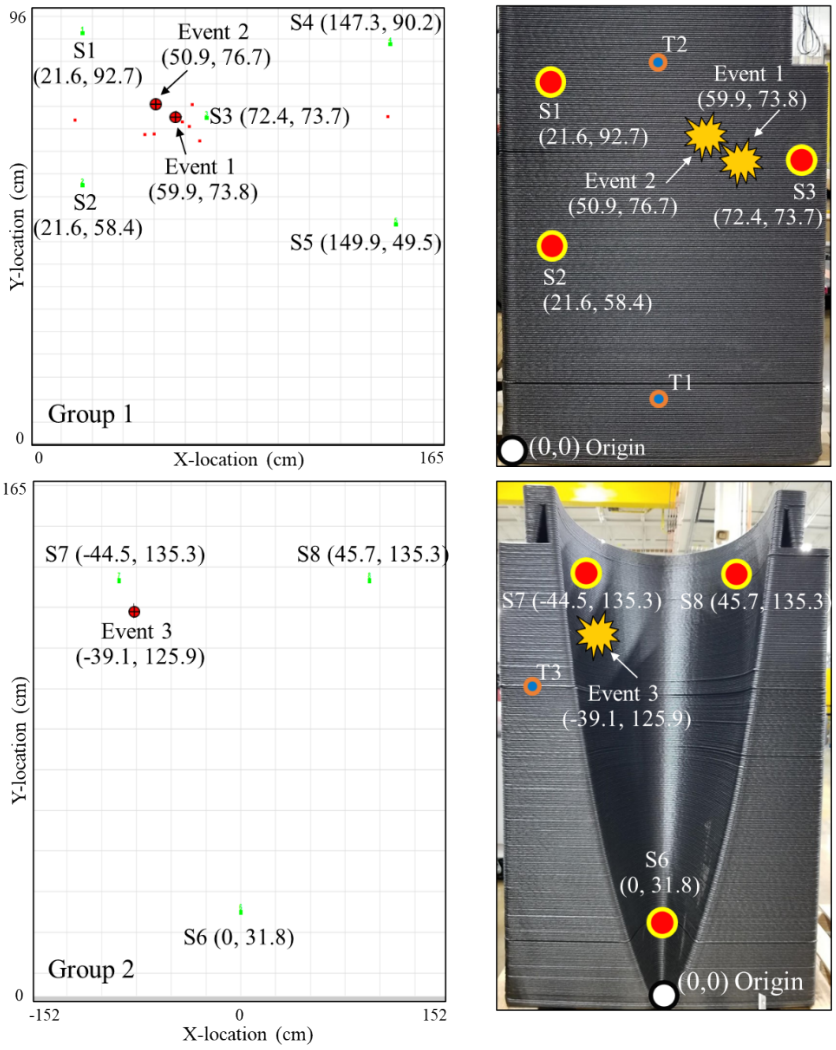

Figure 24: AEwin crack location within Group 1 and 2 (units in cm). Group 1 captured the continuation of crack 1 with Events 1 and 2. Group 2 captured a new crack anomaly with Event 3. Sensors and events overlay on AM structure.

This study offers initial insights into using AE to monitor large composite AM structures for thermal-residual cracking. To confirm the presence of cracks, heat was applied while monitoring thermal expansion using digital image correlation (DIC). This innovative method relies on heat causing cracks to open up due to thermal expansion, which DIC captures in real-time [39, 40]. A convection heat gun served as the heat source, applied to the surface where AE had predicted Event 1 and Event 2 cracks. An optical camera recorded the opening of each crack. The accompanying figure illustrates significant thermal strain occurring at the locations of Event 1 and Event 2. This can be seen in **Figure 25**.

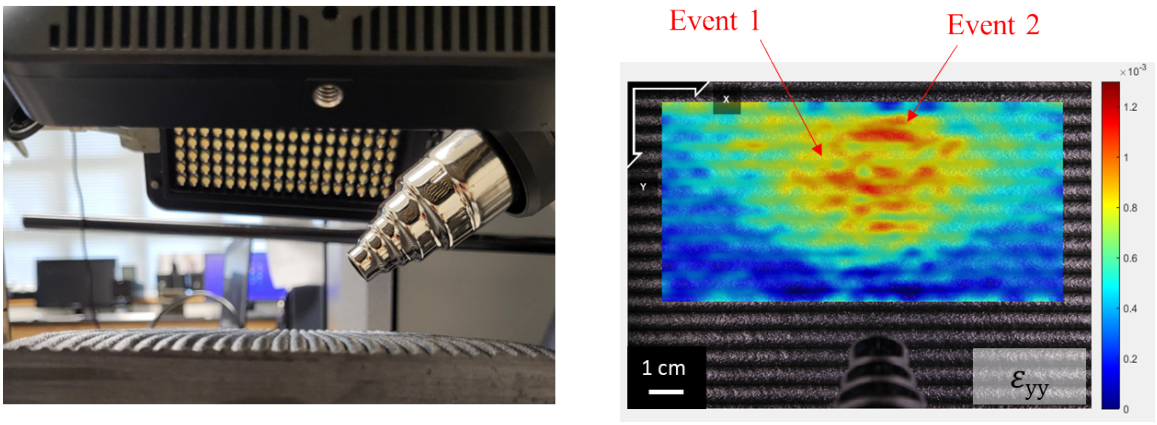

Figure 25: Utilizing digital image correlation (DIC) to monitor the opening of cracks by heating the surface of the AM structure.

1.3 IMPACTS

Large-scale AM is being adapted as a method of producing large composite structures in a short lead time and cost-effective way. With the growing advancement in AM techniques and application a need for the machine monitoring and part qualification is highly needed. There has been leading research focused on the manufacturing, feedstock material but minimum research on the SHM, defect detection, and NDE for AM. Scanning large structure using convictional conventional NDT techniques, such as ultrasound or X-ray, and searching for potential defects can be very time consuming, challenging and cost prohibitive. AE is a passive technique that can be used to monitor and locate defect progression in large structure by distributing group of sensors around the part. This project will utilize AE technique to monitor large-scale AM equipment (i.e. BAAM system located at the MDF/ORNL) and the printed parts it produces. An AE system manufactured/designed by MISTRAS Group will be integrated to the BAAM system. The AE system will provide insight on defect development/progression during and post- the printing process.

1.4 CONCLUSIONS

This project evaluated the use of Acoustic Emission (AE) as a Structural Health Monitoring (SHM) technique for large-scale additive manufacturing (AM). The attenuation study revealed that print orientation significantly impacts acoustic wave propagation in ABS/CF and PSU-PESU/CF materials. 0º direction orientation, with fibers aligned along the deposition direction, exhibited the least attenuation, while the 90º direction showed the most. Perimeter orientation demonstrated minimal attenuation through the print height, typical of perimeter waves. Additionally, the study highlighted the benefits of locally milled surfaces for AE sensor attachment, which provided superior response and minimal signal decay.

Background noise evaluation showed that the deposition extruder head produced a wide range of noise, especially during material runs, while gantry motions had low amplitude responses, indicating minimal interference. This noise data is crucial for developing a signal filtering process to manage extruder noise. Sensor selection and spacing simulations indicated that a broadband PKBBI sensor is optimal for initial monitoring to capture a wide range of frequencies. Subsequently, a narrow-band PK15I sensor should be used to focus on specific frequency ranges, enhancing the detection and analysis of defects. The simulations also determined the necessary sensor spacing to ensure full coverage for large-scale printed structures, considering different material properties.

To validate the ability for AE to capture defected printed components, the technique was used on a large structure which was thermally excited to induce cracking. AE was able to capture three cracking events and determine their locations. An alternative NDT method, digital image correlation (DIC), was utilized to validate and confirm the presence of cracking.

Acoustic emission (AE) offers a passive monitoring technique that can effectively detect and track defect progression in large structures. By strategically placing a network of sensors around the part, AE can monitor structural integrity without disrupting the manufacturing process. This project concludes how to leverage AE technology to monitor the printed components of large-scale AM. The AE system, developed by MISTRAS Group, can be integrated into AM equipment to provide valuable insights into defect development and progression throughout both the printing process and subsequent post-processing stages. This ultimately saves valuable time and cost for the manufacturer and produces a high-quality component for the customer.

1.5 REFERENCES

[1] A. Hassen and M. Kirka, "Additive Manufacturing: The Rise of a Technology and the Need for Quality Control and Inspection Techniques," *Materials Evaluation,* vol. 76, no. 4, pp. 439-453, April 2018.

[2] A. Thompson, I. Maskery and R. Leach, "X-ray computed tomography for additive manufacturing: a review," *Measurement Science and Technology,* vol. 27, no. 072001, p. 17, 2016.

[3] H. Taheri, L. Koester, T. Bigelow and L. Bond, "Thermoelastic Finite Element Modeling of Laser Generated Ultrasound in Additive Manufacturing Materials," in *The American Society for Nondestructive Testing - 2017 Annual Conference*, 2017.

[4] L. Koester, H. Taheri, T. Bigelow, L. Bond and E. Faierson, "In-situ acoustic signature monitoring in additive manufacturing process," in *AIP Conference Proceedings*, 2018.

[5] J. Lee, M. Hassanian, H. Saboonchi, M. Baechle and H. Taheri, "Ultrasonic evaluation of polymer additive manufactured parts for defect inspection and structural integrity assessment," in *SPIE Smart Structures and Nondestructive Evaluation*, California, 2020.

[6] V. Kumar, R. Spencer, T. Smith, J. Condon, P. Yeole, A. Hassen and V. Kunc, "Replacing metal-based lightning strike protection layer of CFRPs by 3D printed electrically conductive polymer layer," *Journal of Advanced Materials,* pp. ISSN 1070-9789, 2020.

[7] R. Spencer, A. Hassen, J. Baba, J. Lindahl, L. Love, V. Kunc, S. Babu and U. Vaidya, "An innovative digital image correlation technique for in-situ process monitoring of composite structures in large scale additive manufacturing," *Composite Structures,* vol. 276, p. 114545, 2021.

[8] B. Compton, B. Post, C. Duty, L. Love and V. Kunc, "Thermal analysis of additive manufacturing of large-scale thermoplastic polymer composites," *Additive Manufacturing,* vol. 17, pp. 77-86, 2017.

[9] H. Saboonchi, D. Ozevin and M. Kabir, "MEMS sensor fusion: Acoustic emission and strain," *Sensors and Actuators A: Physical,* vol. 247, pp. 566-578, 2016.

[10] M. Nunez and H. Saboonchi, "13 - Acoustic emission," in *Techniques for Corrosion Monitoring*, 2nd ed., L. Yang, Ed., Woodhead Publishing , 2021, pp. 305-321.

[11] ASTM E2374-16: Standard Guide for Acoustic Emission System Performance Verification, West Conshohocken, PA: ASTM International, 2016.

[12] ASME Boiler & Pressure Code, "Article 11 and 12," in *Section V - Nondestructive Examination (NDE)*, Edition 2017 ed.

[13] R. Hay, J. Cavaco and V. Mustafa, "Monitoring the civil infrastructure with acoustic emission: bridge case studies," *Journal of Acoustic Emission,* vol. 27, 2009.

[14] B. Dykas and J. Harris, "Acoustic emission characteristics of a single cylinder diesel generator at various loads and with a failing injector," *Mechanical Systems and Signal Processing,* vol. 93, pp. 397-414, 2017.

[15] N. Tziavos, H. Hemida, S. Dirar, M. Papaelias, N. Metje and C. Baniotopoulos, "Structural health monitoring of grouted connections for offshore wind turbines by means of acoustic emission: An experimental study," *Renewable Energy,* vol. 147, no. 1, pp. 13-140, 2020.

[16] J. Tang, S. Soua, C. Mares and T. Gan, "An experimental study of acoustic emission methodology for in service condition monitoring of wind turbine blades," *Renewable Energy,* vol. 99, pp. 170-179, 2016.

[17] H. Yalcinkaya and D. Ozevin, "The design and calibration of particular geometry piezoelectric acoustic emission transducer for leak detection and localization," *Measurement Science and Technology,* vol. 24, no. 9, 2013.

[18] Q. Ai, C. Liu, X. Chen, P. He and Y. Wang, "Acoustic emission of fatigue crack in pressure pipe under cyclic pressure," *Nuclear Engineering and Design,* vol. 240, no. 10, pp. 3616-3620, 2010.

[19] S. Karimian, M. Modarras and H. Bruck, "A new method for detecting fatigue crack initiation in aluminum alloy using acoustic emission waveform information entropy," *Engineering Fracture Mechanics,* vol. 223, no. 106771, 2020.

[20] W. Prosser, M. Gorman and E. Madaras, "Acoustic emission detection of impact damage on space shuttle structures," 2004.

[21] M. Kant, J. Crabtree, S. Young and D. Penumadu, "Concept of limit stress for the tensile behavior of carbon fiber composite tows," *Composites Part B,* vol. 201, 2020.

[22] L. Koester, T. Hossein, T. Bigelow, L. Bond and E. Faierson, "In-situ acoustic signature monitoring in additive manufacturing processes," *AIP Conference Proceedings,* vol. 1949, no. 020006, 2018.

[23] Z. Yang, L. Jin, Y. Yan and Y. Mei, "Filament breakage monitoring in fused deposition modeling using acoustic emission technique," *Sensors,* vol. 18, 2018.

[24] H. Wu, Z. Yu and Y. Wang, "Experimental study of the process failure diagnosis in additive manufacturing based on acoustic emission," *Measurement,* 2018.

[25] L. Love, V. Kunc, O. Rios, C. Duty, A. Elliot, B. Post, R. Smith and C. Blue, "The importance of carbon fiber to polymer additive manufacturing," *J. Mater. Res.,* vol. 29, no. 17, pp. 1893-1898, 2014.

[26] BASF, "Ultrason E, S, P (PESU, PSU, PPSU)".

[27] C. Duty, V. Kunc, B. Compton, B. Post, D. Erdman, R. Smith, R. Lind, P. Lloyd and L. Love, "Structure and mechanical behavior of Big Area Additive Manufacturing (BAAM) materials," *Rapid Prototyping,* vol. 23, no. 1, pp. 181 - 189, 2017.

[28] H. Tekinalp, V. Kunc, G. Velez-Garcia, C. Duty, L. Love, A. Naskar, C. Blue and S. Ozcan, "Highly orientated carbon-fiber-polymer composites via additive manufacturing," *Composites Science and Technology,* vol. 105, pp. 144-150, 2014.

[29] D. Hoskins, S. Kim, A. Hassen, J. Lindahl, V. Kunc and C. Duty, "Modeling thermal expansion of a large area extrusion deposition additively manufactured parts using a non-homogenized approach," in *Solid Freeform Fabrication 2019: Proceedings of the 30th Annual International Solid Freeform Fabrication Symposium - An Additive Manufacturing Conference*, 2019.

[30] K. Billah, H. A.A., A. Nasirov, G. Haye, J. Heineman, V. Kunc and S. Kim, "Thermal Analysis of Large Area Additive Manufacturing Resistance Heating Composites for Out of Oven/Autoclave Applications," in *Proceedings of the ASME 2020 International Mechanical Engineering Congress and Exposition*, Virtual, Online, November 16-19, 2020.

[31] Y. Zhang, "Measuring Acoustic Attenuation of Polymer Materials Using Drop Ball Test," Embry-Riddle Aeronautical University, 2013.

[32] S. Yuyama and M. Ohtsu, "Failure Detection of High-Strength Tendons in Prestressed Concrete Bridges by AE," *Concrete Research Letters,* vol. 2, no. 3, pp. 295-299, 2011.

[33] K. Niroua, "Acoustic Monitoring of the Main Suspension Cables of the Anthony Wayne Bridge," 2014.

[34] P. Yeole, S. Kim, A. Hassen, V. Kumar, V. Kunc and U. Vaidya, "Large-scale additive manufacturing tooling for extrusion-compression molds," *Additive Manufacturing Letters,* vol. 1, p. 100007, 2021.

[35] Techmer PM, "Electrafil® ABS 1501 3DP," 01 May 2024. [Online]. Available: https://catalog.ides.com/Datasheet.aspx?I=46454&E=391538.

[36] Techmer PM, "Electrafil® PESU 1810 3DP," 01 May 2024. [Online]. Available: https://catalog.ides.com/Datasheet.aspx?I=46454&E=391538.

[37] S. Kore, R. Spencer, H. Ghossein, L. Slaven, D. Knight, J. Unser and U. Vaidya, "Performance of hybridized bamboo-carbon fiber reinforced polypropylene composites processed using wet laid technique," *Composites Part C: Open Accesss,* vol. 6, p. 100185, 2021.

[38] Physical Acoustics Corporation, "PCI-2 Based AE System - User's Manual - Rev 3," Physical Acoustics Corporation, Princeton Junction, NJ, 2007.

[39] R. Spencer, A. Hassen and U. Vaidya, "Fiber Orientation Evaluation in Reinforced Composites using Digital Image Correlation," in *American Society for Nondestructive Testing Research Symposium*, April 2021.

[40] R. Spencer, S. Alwekar, E. Jo, A. Hassen, S. Kim and U. Vaidya, "Fiber Orientaiton Evaluation in Reinforced Composites using Digital Image Correlation and Thermal Excitation," *Composites Part B: Engineering,* vol. 234, p. 109713, 2022.

[41] B. Conner, G. Manogharan, A. Martof, L. Rodomsky, C. Rodomsky, D. Jordan and J. Limperos, "Making sense of 3-D printing: Creating a map of additive manufacturing products and services," *Additive Manufacturing,* pp. 64-76, 2014.

[42] V. Kunc, A. Hassen, J. Lindahl, S. Kim, B. Post and L. Love, "Large Scale Additively Manufactured Tooling for Composites," in *15th Japan International SAMPE Symposium and Exhibition*, Tokyo, 2017.

[43] A. Hassen, R. Springfield, J. Lindahl, B. Post, L. Love, C. Duty, V. Vaidya, R. Pipes and V. Kunc, "The Durability of Large-Scale Additive Manufacturing Composite Molds," in *CAMX - The Composite and Advanced Materials Expo*, Anaheim, CA, 2016.

[44] Local Motors, "Meet Olli," Local Motors , [Online]. Available: https://localmotors.com/meet-olli/.

[45] E. Peterson, "Technical Challenges to Adopting Large Scale Additive Manufacturing for the Production of Yacht Hulls," in *International Conference on Human Systems Engineering and Design III*, 2020.

[46] B. Post, B. Richardson, R. Lind, L. Love, P. Lloyd, V. Kunc, B. Rhyne, A. Roschli, J. Hannan, S. Nolet, K. Veloso, P. Kurup, T. Remo and D. Jenne, "Big Area Additive Manufacturing Applications In Wind Turbine Molds," in *Solid Freeform Fabrication - An Additive Manufacturing Conference*, 2017.

[47] S. Kim, H. Baid, A. Hassen, A. Kumar, J. Lindahl, D. Hoskins, C. Ajinjeru, C. Duty, P. Yeole, U. Vaidya, F. Abdi, L. Love, S. Simunovic and V. Kunc, "Analysis on part distortion and residual stress in big area additive manufacturing with carbon fiber-reinforced thermoplastic using dehomogenization technique," in *CAMX Conference Proceedings*, Anaheim, CA, 2019.

[48] H. Taheri, L. Koester, T. Bigelow, L. Bond, D. Braconnier, E. Carcreff, G. Dao, A. Clauder and A. Hassen, "Fast Ultrasonic Imaging with Total Focusing Method (TFM) for Inspection of Additively Manufactured Polymer Composite Component," in *ASNT 27th Research Symposium*,

FL, USA, 2018.

2. PARTNER BACKGROUND

MISTRAS Group is a leading "one source" multinational provider of integrated technology-enabled asset protection solutions, helping to maximize the safety and operational uptime for civilization’s most critical industrial and civil assets. MISTRAS has ~5,400 employees across 115 locations worldwide, targeting key markets including oil & gas, aerospace, power, infrastructure, and manufacturing. Their consolidated sales nets to $270M USD.